

Atomic Alignment in PbS Nanocrystal Superlattices with Compact Inorganic Ligands via Reversible Oriented Attachment of Nanocrystals

Ahhyun Jeong,¹ Aditya N. Singh,² Josh Portner,¹ Xiaoben Zhang,¹ Saghar Rezaie,³ Justin C. Ondry,¹ Zirui Zhou,¹ Junhong Chen,¹ Ye Ji Kim,¹ Richard D. Schaller,^{4,5} Youssef Tazouli,¹ Zehan Mi,¹ Sadegh Yazdi,³ David T. Limmer,^{2,6,7} and Dmitri V. Talapin^{1,4,*}

¹*Department of Chemistry, James Franck Institute, and Pritzker School of Molecular Engineering, University of Chicago, Chicago, Illinois 60637, United States*

²*Department of Chemistry, University of California, Berkeley, California 94720, USA*

³*Renewable and Sustainable Energy Institute, University of Colorado, Boulder, Colorado, USA*

⁴*Center for Nanoscale Materials, Argonne National Laboratory, Argonne, Illinois 60439, United States*

⁵*Department of Chemistry, Northwestern University, Evanston, Illinois, USA*

⁶*Chemical Sciences and Materials Sciences Divisions,*

Lawrence Berkeley National Laboratory, Berkeley, California 94720, USA

⁷*Kavli Energy NanoSciences Institute, University of California, Berkeley, California 94720, USA*

(Dated: January 21, 2026)

Nanocrystals (NCs) serve as versatile building blocks for the creation of functional materials, with NC self-assembly offering opportunities to enable novel material properties. Here, we demonstrate that PbS NCs functionalized with strongly negatively charged metal chalcogenide complex (MCC) ligands, such as $\text{Sn}_2\text{S}_6^{4-}$ and AsS_4^{3-} , can self-assemble into all-inorganic superlattices with *both* long-range superlattice translational and atomic-lattice orientational order. Structural characterizations reveal that the NCs adopt unexpected edge-to-edge alignment, and numerical simulation clarifies that orientational order is thermodynamically stabilized by many-body ion correlations originating from the dense electrolyte. Furthermore, we show that the superlattices of $\text{Sn}_2\text{S}_6^{4-}$ -functionalized PbS NCs can be fully disassembled back into the colloidal state, which is highly unusual for orientationally attached superlattices with atomic-lattice alignment. The reversible oriented attachment of NCs, enabling their dynamic assembly and disassembly into effectively single-crystalline superstructures, offers a pathway toward designing reconfigurable materials with adaptive and controllable electronic and optoelectronic properties.

INTRODUCTION

Self-assembly of nanocrystals (NCs) enables the bottom-up design of a wide range of structures from a library of NCs as building blocks.^{1,2} Extensive work has established formation of a library of different structures built from NCs, including close-packed structures,³ multicomponent crystalline and quasi-crystalline structures,^{4–7} and chiral structures.^{8,9} When NCs organize themselves into densely-packed superlattices with long-range order, they can exhibit collective phenomena. For instance, electronic coupling within superlattices can lead to miniband formation, enhanced charge carrier mobility, and collective optical effects such as super-fluorescence and superradiance.¹⁰ These emergent properties expand the functional landscape of NC materials, opening avenues for advanced optoelectronic applications, quantum technologies, and nanoscale sensing.^{1,2}

Traditional approaches for NC self-assembly rely on surface functionalization to control pair potentials between NCs, superlattice phase behavior or to enable stimuli-responsive assembly and disassembly. For example, length and coverage of organic ligands can be tuned

to access different superlattice phases,^{11–15} and DNA-based functionalization enables self-assembly of NCs into programmable architectures.^{16–19} Chemically- or photo-responsive ligands further enable external control of assembly and disassembly processes.^{8,20–22} While these ligands maintain colloidal stability and direct assembly, they also act as insulating barriers that suppress interparticle coupling in the resulting superlattices.²³ Switching to shorter ligands or removing them entirely can facilitate direct NC contact and strong coupling but often drives irreversible aggregation or oriented attachment preventing reversibility of the assembly process and restricting long-range ordering of NCs.^{24–26} These challenges reveal the pressing need for alternative strategies that enable both strong electronic coupling and structural adaptability in NC superlattices.

One promising direction is the use of short, compact inorganic ligands to functionalize NCs, replacing their organic counterparts. These inorganic ligands substantially reduce interparticle spacing, allowing for enhanced electronic coupling and potentially new regimes of collective behavior.^{27–30} However, unlike organic ligands, inorganic species stabilize NCs predominantly through electrostatic interactions, introducing a fundamentally different mechanism for both colloidal stability and self-assembly.^{31–33} For this reason, the self-assembly of electrostatically stabilized NCs remains relatively underexplored. A deeper

* Corresponding author: dvtalapin@uchicago.edu

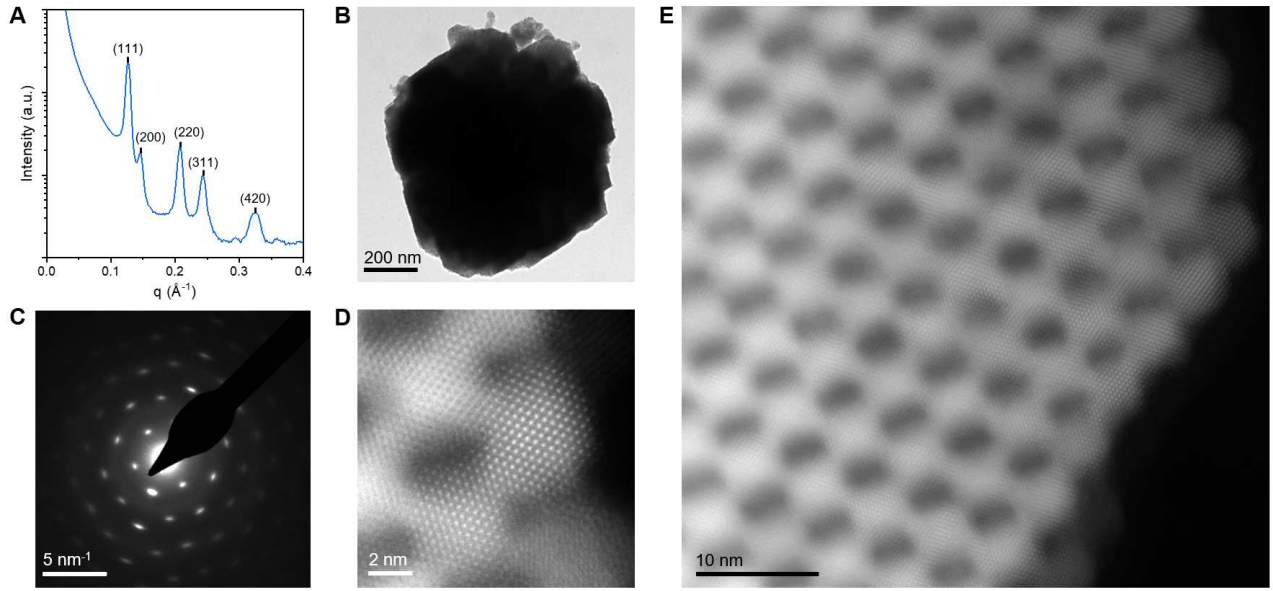


FIG. 1. (A) Small-angle X-ray scattering (SAXS) pattern of 5.7 nm $\text{PbS-Sn}_2\text{S}_6^{4-}$ nanocrystal (NC) superlattice. The peak assignment shows that the superlattice adopts a face-centered cubic (*fcc*) structure. (B) Bright-field transmission electron microscopy (TEM) image of a 5.7 nm $\text{PbS-Sn}_2\text{S}_6^{4-}$ NC superlattice domain. (C) Selected area electron diffraction (SAED) image of the entire grain. Distinct spot patterns indicate that the PbS NCs are atomically aligned. (D, E) Scanning transmission electron microscopy (STEM) high-angle annular dark-field (HAADF) image of a 5.7 nm $\text{PbS-Sn}_2\text{S}_6^{4-}$ NC superlattice.

understanding of this approach is critical, as it holds promise for creating functional superlattices with robust collective electronic, optical, and structural properties.

In this study, we demonstrate the self-assembly of PbS NCs with metal chalcogenide complex (MCC) ligands (e.g. $\text{Sn}_2\text{S}_6^{4-}$, AsS_4^{3-}) into all-inorganic superlattices exhibiting both long-range translational *and* orientational order, with individual NCs bridged with epitaxial “necks”. We show that the self-assembly of these NCs exhibits controllable reversibility, a counterintuitive feature for orientationally attached NC superlattices with atomic-lattice alignment. Structural characterizations reveal that the NCs adopt an edge-to-edge alignment, a unique configuration facilitated by strong ionic correlations in the dense electrolyte. The formation of densely packed and oriented superlattices with controlled reversibility offers possibilities to utilize the benefits of reversible self-assembly in dynamic and adaptive material systems.

RESULTS AND DISCUSSION

Self-assembly of nanocrystals with charged surfaces into superlattices featuring translational and atomic-lattice orientational order

Monodisperse PbS NCs with various sizes (5.4 ± 0.3 , 5.7 ± 0.3 , 7.3 ± 0.7 , 8.3 ± 0.5 nm) were synthesized from lead oleate and substituted thioureas using the methods

developed by the Owen group (Figure S1).³⁴ The surface oleate (OA) ligands of the PbS NCs are then substituted with thiostannate ligands ($\text{Sn}_2\text{S}_6^{4-}$) by stirring them with a solution of $\text{K}_4\text{Sn}_2\text{S}_6$ in N-methylformamide (NMF). After stirring overnight, the PbS NCs transfer to the NMF phase, indicating the substitution of OA ligands by $\text{Sn}_2\text{S}_6^{4-}$ ligands. Small-angle X-ray scattering (SAXS) patterns of $\text{Sn}_2\text{S}_6^{4-}$ -capped PbS NCs ($\text{PbS-Sn}_2\text{S}_6^{4-}$ NCs), in addition to oscillations originating from the spherical form factor of individual NCs, exhibit a broad peak in the low- q region ($q < 0.1 \text{ \AA}^{-1}$), indicative of long-range repulsive forces between the particles due to the presence of highly charged surface ligands (Figure S2).³² The absence of a low- q upturn confirms that the particles are free of aggregation. Similar SAXS patterns were observed for MCC-capped PbS NCs of different sizes, and with different charged surface ligands (Figure S2).

The self-assembly of $\text{PbS-Sn}_2\text{S}_6^{4-}$ NCs colloidally dispersed in NMF was induced by adding a non-solvent and a flocculant that screened the surface potential of the $\text{PbS-Sn}_2\text{S}_6^{4-}$ NCs, reducing long-range electrostatic repulsion between NC surfaces.³⁰ As a flocculant, we used K_3AsS_4 , K_4GeS_4 or $\text{K}_4\text{Sn}_2\text{Se}_6$ that dissociate in polar solvents greatly increasing the ionic strength. Additionally, a non-solvent (e.g., DMF, MeCN) lowers the solvent dielectric constant further facilitating self-assembly by decreasing the solubility of $\text{PbS-Sn}_2\text{S}_6^{4-}$ NCs. A black solid precipitates out of the solution, leaving unassembled $\text{PbS-Sn}_2\text{S}_6^{4-}$ NCs remaining as a brown supernatant. To wash as-prepared 5.7 nm $\text{PbS-Sn}_2\text{S}_6^{4-}$ NC superlat-

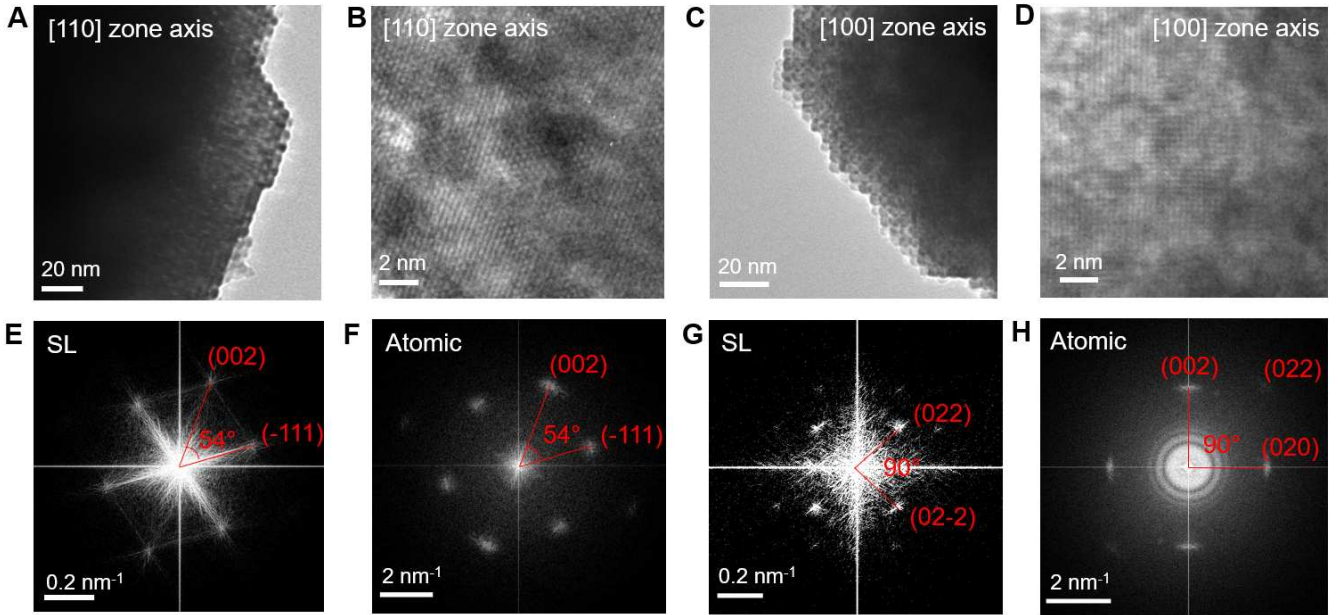


FIG. 2. (A) Transmission electron microscopy (TEM) and (B) High-resolution TEM (HRTEM) image of the superlattice of 5.7 nm $\text{PbS-Sn}_2\text{S}_6^{4-}$ NCs, viewed along the (110) zone axis. (C) TEM and (D) HRTEM images of the superlattice of the same NC superlattice viewed along the (100) zone axis. (E, F) Fourier-transformed TEM (FT-TEM) images of the superlattice viewed along the (110) zone axis, with the distinct spots indicating highly ordered *fcc* structures at both nanometer and atomic scales. (G, H) FT-TEM of the superlattice viewed along the (100) zone axis, also with distinct spots indicating a high degree of *fcc* ordering.

tic, the collected precipitate was suspended in acetonitrile, followed by centrifugation to remove the solvent. The residual acetonitrile was then allowed to evaporate, yielding washed superlattice as a free-flowing black solid powder. The SAXS pattern of the precipitated solid revealed that they consist of highly ordered superlattices, evidenced by the emergence of sharp Bragg peaks (Figures 1A and S3), while the photoluminescence (PL) spectrum of the superlattice confirms that the quantum confinement in the NCs is preserved (Figure S4). Our findings suggest that various multivalent salts can function as flocculants, and different solvents miscible with NMF and having a lower polarity than NMF can act as the non-solvent (Figure S3). Consistent Bragg peak patterns were observed when various flocculants and non-solvents were used, indicating that these factors do not substantially affect the superlattice crystal structure. Additionally, $\text{PbS-Sn}_2\text{S}_6^{4-}$ NCs ranging from 5.4 nm to 8.1 nm in size also self-assembled into superlattices (Figure S5), with shifts in Bragg peaks along the *q*-axis corresponding to expanded lattice constants as NC diameter increases. PbS NCs with another charged ligand (AsS_4^{3-}) were also able to be self-assembled into an ordered superlattice under the same experimental conditions (Figure S5).

Figure 1 demonstrates that $\text{PbS-Sn}_2\text{S}_6^{4-}$ NCs self-assemble into superlattices exhibiting not only translational but also orientational order of NCs. Figure 1A

presents a SAXS pattern of washed 5.7 nm $\text{PbS-Sn}_2\text{S}_6^{4-}$ NC superlattices. The Bragg peak assignment indicates that the superlattice adopts a face-centered cubic (*fcc*) structure (Figure S6). Figures 1B and 1C show transmission electron microscopy (TEM) and corresponding selected area electron diffraction (SAED) pattern of washed 5.7 nm $\text{PbS-Sn}_2\text{S}_6^{4-}$ NC superlattices, respectively. The SAED pattern consists of distinct spot patterns that correspond to an *fcc* atomic lattice viewed at (110) zone axis (Figure S7). The absence of rings or unidentified spots in the SAED data indicates that the PbS NCs maintain orientational order throughout the entire superlattice. Additional TEM and SAED images can be found in Figure S8. High-angle annular dark-field scanning transmission electron microscopy (HAADF-STEM) imaging with atomic resolution (Figures 1D, 1E, and S9) reveals the crystalline necks between NCs formed across the superlattice. To rule out the possibility of projection artifact coming from NCs in different layers, the high-resolution STEM images were acquired with a relatively large convergence angle (25 mrad), which provides depth sensitivity on the order of a few nanometers, comparable to the NC size. If the particles were at different heights, they would not both be in focus. Furthermore, during STEM imaging of these superlattices (beam current less than 50 pA), we did not observe any changes that would suggest the electron beam is inducing the crystalline con-

nections (necks). Additional TEM images of the superlattices show that spontaneous oriented self-assembly occurs for $\text{PbS-Sn}_2\text{S}_6^{4-}$ NCs of different sizes (Figure S10), and similar behavior can be found from PbS-AsS_4^{3-} NCs and $\text{PbSe-Sn}_2\text{S}_6^{4-}$ NCs (Figure S11). The coherence of the atomic lattice across the superlattice is further supported by the Scherrer analysis of the diffraction spots in SAED patterns – the Scherrer size of atomic crystalline domains in the superlattice exceeds both the Scherrer size and SAXS diameter of individual PbS NCs (Figures S12-S16).

Some degree of orientational alignment is often observed in self-assembled NC superlattices, typically associated with NC faceting and parallel facet alignment in superlattices that maximizes NC packing density.³⁵ However, the soft nature of the organic surface ligands cannot tightly lock the NC alignment, and SAED patterns typically show diffraction arcs rather than spots typical for single crystals.³⁶ An important exception is the assembly of colloidal NCs at the liquid/liquid interface, followed by the removal of surface ligands—the oriented attachment of NCs can locally create a comparable order of the atomic lattices through irreversible NC necking.^{25,26} There, the liquid-liquid interface plays an important role for in-plane alignment of NCs and gentle removal of surface ligands to induce the oriented attachment. To the best of our knowledge, the orientational ordering of sub-10 nm NCs in large 3D NC superlattices shown in Figure 1 is rather unprecedented and requires further investigation.

Structural analysis of $\text{PbS-Sn}_2\text{S}_6^{4-}$ nanocrystal superlattices

The translational and orientational ordering of the 5.7 nm $\text{PbS-Sn}_2\text{S}_6^{4-}$ NCs was further examined using real and reciprocal space analysis of TEM images of NC superlattices. Figure 2 presents TEM and Fourier-transformed (FT) TEM images of 5.7 nm $\text{PbS-Sn}_2\text{S}_6^{4-}$ NC superlattice. Figures 2A and 2B are the low-magnification TEM and high-resolution TEM (HRTEM) images of the resulting superlattice, while Figures 2E and 2F display the corresponding FT-TEM images, respectively. The FT-TEM image in Figure 2E reflects the periodicity of NC packing in the superlattice, showing six spots arranged in an elongated hexagonal pattern, where two adjacent spots form a 54° angle. This arrangement is characteristic of the reciprocal-space representation of a face-centered cubic (*fcc*) crystal viewed along the (110) zone axis, which is consistent with the SAXS pattern (Figure 1A).³⁷ The four innermost spots arise from the (-111), (1-11), (-11-1), and (1-1-1) sets of superlattice planes, while the two outer spots correspond to the (002) and (00-2) planes. The calculation of the *d*-spacing from the spot-to-center distances yields a superlattice unit cell

length of 8.7 nm, which is consistent with the SAXS measurement of 8.5 nm. The FT-TEM image in Figure 2F indicates a PbS atomic unit cell lattice constant of 6.1 Å, which is in good agreement with the powder X-ray diffraction (PXRD) measurement (5.9 Å, Figure S13). The TEM, HRTEM, and the corresponding FT-TEM images of the 5.7 nm $\text{PbS-Sn}_2\text{S}_6^{4-}$ NC superlattice viewed along (100) zone axis are shown in Figures 2C, 2D, 2G, and 2H, respectively.

Analysis of PXRD patterns of 5.7 nm $\text{PbS-Sn}_2\text{S}_6^{4-}$ NCs provides an average $h(111)/h(100)$ Wulff construction ratio of 1.02 (Figure S13), indicating that these NCs exhibit a truncated octahedral shape ($0.58 < h(111)/h(100) < 1.15$),³⁸ consistent with previous experimental and computational studies.^{38,39} TEM images of colloidal $\text{PbS-Sn}_2\text{S}_6^{4-}$ NCs show that the NCs are nearly spherical, which further supports this (Figure S17). A model of a truncated octahedral NC is shown in Figure 3A. The FT-TEM images in Figures 2E and 2F demonstrate that both the NC superlattice and the atomic lattices of individual NC are simultaneously oriented along the (110) zone axis. This alignment is only achievable if the PbS NCs are assembled edge-to-edge, with the closest nearly touching edges being parallel to the <110> set of equivalent lattice directions of the superlattice and NC atomic lattices, as depicted in Figures 3B and 3E. Furthermore, the matching spot patterns in the FT-TEM images in Figures 2D and 2H for the superlattice viewed along the (100) zone axis further confirm the edge-to-edge alignment of NCs within the superlattice, as depicted in Figures 3C and 3F.

This edge-to-edge alignment is highly unusual for NC assemblies, which typically favor face-to-face orientations to maximize the cohesive energy from van der Waals interactions. For NCs with steric colloidal stabilization provided by ligands with long hydrocarbon chains, there are only a few reported examples of superlattices supported by vertex-to-vertex contacts,⁴⁰ but such examples are far rarer compared to the face-to-face assemblies. We propose that this unique superlattice configuration plays a key role in enabling the reversible nature of self-assembly processes in the absence of bulky organic surface ligands—the traditional face-to-face packing would be more prone to irreversible aggregation under strong van der Waals forces. Furthermore, the narrow connecting NC edges may be instrumental in establishing epitaxial necks with atomically precise order (Figure 1D and 1E) as discussed below.

Theoretical insight into the origin of edge-to-edge orientation in $\text{PbS-Sn}_2\text{S}_6^{4-}$ nanocrystal superlattices

In this Section, we introduce a theoretical model helping to elucidate possible origin of the edge-to-edge orientation in our NC superlattices. Such edge-to-edge ori-

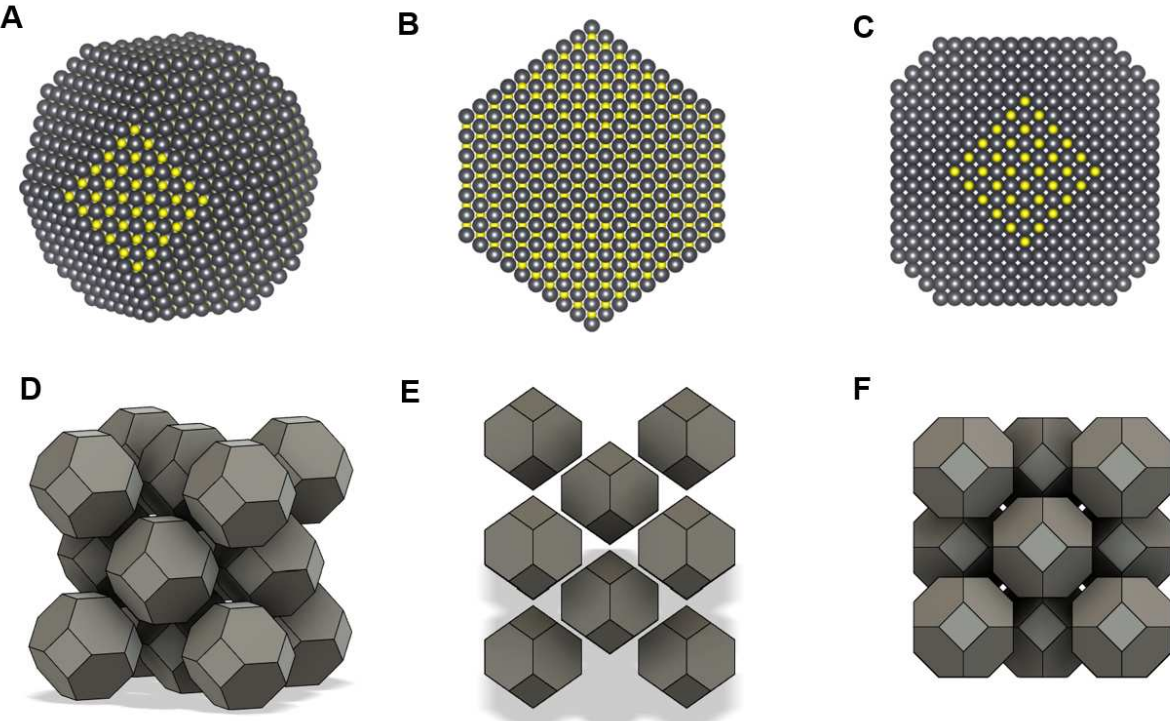


FIG. 3. (A) Illustration of 5.7 nm $\text{PbS-Sn}_2\text{S}_6^{4-}$ NC superlattice. Illustration of the superlattice viewed along (B) (110) zone axis and (C) (100) zone axis. (D) Illustration of the PbS NC viewed along (E) (110) zone axis and (F) (100) zone axis.

entation is very unusual not only in experimental but also in computational studies of NC self-assembly.⁴¹ The simulations of self-assembly of nanoparticles with conventional bulky organic ligands have shown superlattices with various kinds of orientational order, but not edge-to-edge or vertex-to-vertex arrangements, because of the van der Waals attraction strongly favoring face-to-face contacts.^{35,42} Intriguingly, calculations using combination of mean-field electrostatic repulsion and van der Waals attraction (e.g. DLVO theory) predict that electrostatically stabilized nanoparticles, e.g., truncated octahedra, also adopt face-to-face orientation.⁴³⁻⁴⁵ The discrepancy between the previous computational studies of NC self-assembly and the experimentally observed edge-to-edge alignment in $\text{PbS-Sn}_2\text{S}_6^{4-}$ NC superlattices may arise from the fundamental limitations of DLVO theory, which is strictly applicable to colloids suspended in dilute 1:1 electrolytes and ignores ionic correlations present in concentrated electrolyte solutions, which are particularly strong for multivalent ions.^{46,47}

To address this limitation, we develop a theoretical model accounting for ionic correlations in a system of highly charged colloidal particles in a solution of multivalent ions. The theoretical framework combines phenomenological Landau-Ginzburg field theory adapted for describing strongly correlated ionic systems^{48,49}, with explicit geometric descriptions of truncated octahedral NCs and numerical solution of the resulting Euler-Lagrange

equations. Full technical details are provided in Section 5 of Supporting Information. The effective Hamiltonian, which serves as a basis for calculating the free energy of a system, accounts for (i) short-range interactions including dispersion forces and steric effects; (ii) long-range Coulomb interactions. The former term describes local structure with the characteristic length scale l_c determined by ion and solvent size, while the second contribution accounts for the electrostatic screening with characteristic length l_s closely related to the Debye screening length. This approach has been successfully employed to rationalize interparticle forces in highly charged colloidal systems in concentrated electrolytes such as molten salts and ionic liquids.^{49,50}

This model predicts that the response of the electrolyte to a localized charge, the susceptibility $\chi(r)$, has the form of a damped oscillation^{48,49}:

$$\chi(r) = \frac{A}{4\pi r} \exp\left(-\frac{\alpha}{r}\right) \cos\left(\frac{\gamma r}{\alpha} - \theta\right),$$

where A , α , γ and θ are simple analytic functions of l_c and l_s :

$$\alpha = 2l_c l_s^{1/2} (2l_c - l_s)^{-1/2}, \quad \gamma = \sqrt{\frac{2 + l_s/l_c}{2 - l_s/l_c}},$$

$$\theta = \sin^{-1}(l_s/2l_c), \quad A = \frac{1}{al_c \sqrt{4l_c^2 - l_s^2}}$$

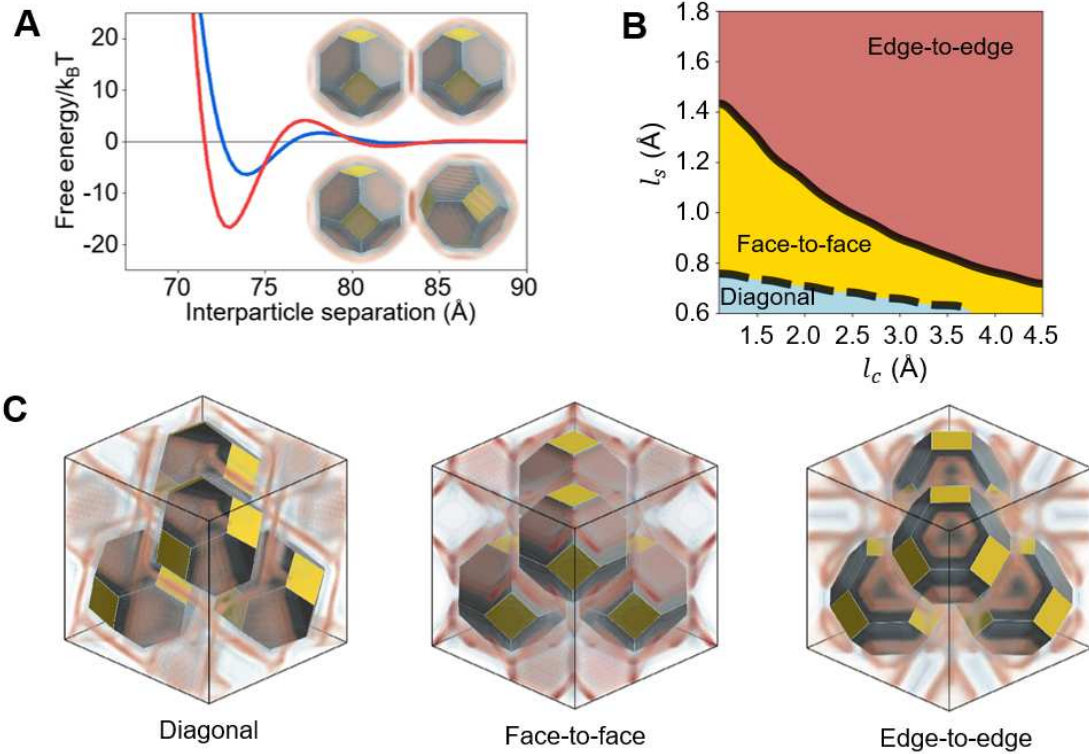


FIG. 4. (A) Free energy difference between two aligned (red line) and nonaligned (blue line) nanocrystals (NCs) as a function of the distance of separation. Top and bottom inset show the asymmetric charge density for the aligned and non-aligned NCs at the distance of minimum free energy. B) Phase diagram for orientational order in a four-site *fcc* lattice as a function of characteristic length scales related to ion and solvent size (l_c) and screening length (l_s). The three phases correspond to diagonal alignment (blue), face-to-face alignment (gold) and edge-to-edge alignment (red). (C) Representative snapshots of the three phases along with the asymmetric charge density. The snapshot consists of truncated octahedral PbS NCs and the charge distributions around the NCs. Red indicates positive charge, blue indicates negative charge.

The plots of susceptibility $\chi(r)$ in respect to interparticle distance (r) are shown in Figure S18. The oscillatory component arises from the formation of alternating layers of cations and anions in the vicinity of a charged surface, which results from the competition between ionic packing constraints and the requirement for local charge neutrality.⁵¹⁻⁵⁴ The oscillation period is related to ion size and spacing, and the oscillation amplitude decays away from the interface over a distance α . These model parameters are directly tied to familiar experimental tuning knobs. Thus, the electrolyte ionic strength and ion valency control the screening length l_s (shorter at higher ionic strength or higher ion charge). Solvent dielectric constant and temperature: high- ϵ solvents and higher temperatures lead to longer l_s and more extended ion layering. Ion size controls the short-range correlation length l_s , which sets the length scale for layering. Ligand surface charge density determines the magnitude of the electrolyte-mediated NC-NC interaction, which strongly increases with more highly charged ligands. In this way, the model provides a direct link between chemically controllable parameters (salt concentration, solvent, ligand

chemistry, NC size and shape) and the emergent orientational order and interactions in NC superlattices mediated by strong electrolytes.

The susceptibility $\chi(r)$ is the kernel that generates the pair potential $W(r)$ between NCs. In the simplest approximation of NC as a point, the pair potential between NCs is directly proportional to $-\chi(r)$. To account for the NC size and shape (truncated octahedron), we introduce surface and volume form factors and derive analytic expressions for these form factors^{55,56}. Charged ligands at the NC surface are modeled as an effective surface field with the strength controlled by a parameter directly related to the surface charge density of the ligands. This approach enables us to directly calculate the solvent contribution to the total free energy for any given position and orientation of the NCs.

Figure 4A shows the free energy profile for two 5.7 nm truncated octahedral NCs as a function of their separation distance. The red curve represents the free energy when the two PbS NCs are orientationally aligned, whereas the black curve illustrates the case where they are tilted with respect to each other. In both configurations, we observe short-ranged free energy oscillatory

decay with increasing separation. This behavior arises from the oscillatory charge profiles that surround NCs in solution. As two NCs approach, the overlap of these profiles results in constructive or destructive interference, resulting in minima (in-phase) and maxima (out-of-phase) in the free energy landscape. Additionally, we find that the faceted geometry of PbS NCs leads to pronounced anisotropy in their interactions, evidenced by the strong dependence of the free energy profile on relative orientation. These findings suggest that the driving force for orientational ordering in PbS NCs is rooted in the structured layering of ligands and cations within the superlattice.

Next, we carry out Monte Carlo (MC) simulations to explore the orientational alignment of four truncated octahedral NCs arranged on the sites of an *fcc* lattice with the lattice constant of 90 Å. By performing iterative free energy calculations, we determined the most energetically favorable configuration that minimizes the free energy (Figures S19 and S20). The robustness of the model is further validated using a larger supercell containing 32 NCs (Figure S20). These simulations produced a detailed orientational phase diagram (Figure 4B), illustrating the relationship between the decay length (α) and the oscillation parameter (γ), which are set by l_c and l_s . The diagram reveals three distinct ordered states: diagonal alignment, face-to-face alignment, and the experimentally observed edge-to-edge alignment (Figure 4C). This diverse orientational landscape arises from charge layering effects in solutions containing multivalent ions, which strongly influence free energy as a function of orientation. The edge-to-edge configuration is thermodynamically preferred over a wide parameter range and becomes exclusively favored as the decay length (α) increases. These findings highlight the crucial role of long-range electrostatic interactions with charge layering effects in stabilizing the edge-to-edge orientation.

Reversible oriented attachment of edge-to-edge assembled PbS-Sn₂S₆⁴⁻ nanocrystals

In this Section, we focus on the formation of epitaxial “necks” between PbS-Sn₂S₆⁴⁻ NCs (Figure 1D). This process resembles oriented attachment of NCs.²⁴ Oriented attachment is common for nanoscale crystals, while it is rarely observed for large crystals because joining two crystals together requires rearranging a number of surface atoms roughly proportional to the areas of merging surfaces. Oriented attachment can be an ideal approach to establish strong electronic coupling within NC superlattices.^{25,26} However, a major limitation of oriented attachment as universal mechanism for assembling nanoscale building blocks into meso- and macroscale objects with near-atomic precision is the lack of micro-reversibility required for healing occasional bonding mis-

takes. For example, a NC superlattice in Figure 1A contains about $3 \cdot 10^6$ individual PbS-Sn₂S₆⁴⁻ NCs. It is highly likely that the formation of such a complex construct requires numerous rearrangements. In traditional crystal growth, the reversible bonding and surface mobility of added building blocks are critical for maintaining structural coherence.⁵⁷ However, disassembly of a crystalline “neck” between NCs is highly improbable because of a large total energy of all chemical bonds that need to be broken, thus making traditional oriented attachment a “forward-only” process.

Counterintuitively, Figure 5 demonstrates that self-assembled PbS-Sn₂S₆⁴⁻ NC superlattices can be fully reversed to the colloidal state. The SAXS pattern of a colloidal solution of 5.7 nm PbS-Sn₂S₆⁴⁻ NCs is shown as the black line in Figure 5A. The red line corresponds to a representative SAXS pattern of a superlattice formed using dimethylformamide (DMF) as the non-solvent and K₃AsS₄ as the flocculant. After centrifugation to remove solvents and unassembled NCs, the residual solid was collected for SAXS measurements of the as-prepared superlattices. The sharp Bragg peaks in the SAXS pattern confirm the formation of a highly ordered *fcc* superlattice with a unit cell length of 9.3 nm (Figure S21). This PbS-Sn₂S₆⁴⁻ NC superlattice can be disassembled back into colloidal NCs by adding highly polar NMF solvent (Figure S22). The SAXS pattern of the redispersed PbS-Sn₂S₆⁴⁻ NCs, shown as the blue line in Figure 5A, exhibits identical Bessel oscillations in the high-*q* region, ($q > 0.1 \text{ \AA}^{-1}$) to those in the original colloidal solution, thus confirming that the PbS NCs were fully recovered with no changes in size or shape distribution. This reversible self-assembly remained effective even after the superlattices were aged for over two days prior to redispersion (Figure S23). TEM images of the original solution of PbS-Sn₂S₆⁴⁻ NCs and the solution obtained by redissolving a superlattice (Figure S24) further confirm complete disassembly of superlattices into individual NCs.

TEM and HRTEM images of as-prepared superlattices display continuous atomic lattice fringes, indicating strong orientational alignment of PbS NCs (Figure 5C). Washing these superlattice with excess acetonitrile does not change the qualitative appearance of the superlattices in TEM and HRTEM images (Figure 5D), while making them more robust and less prone to electron beam damage. The washing causes a lattice contraction of the 5.7 nm PbS-Sn₂S₆⁴⁻ NC superlattice from 9.3 nm to 8.5 nm, evidenced by the shift of Bragg peaks in the SAXS patterns to lower *q*-values after washing (Figure 5B). Immediately after washing with acetonitrile, the superlattices can be redissolved into individual NCs, but lose solubility upon aging in dry state. Attempts to redisperse washed and aged PbS-Sn₂S₆⁴⁻ NC superlattices in NMF (Figure S25) result in SAXS patterns with Bragg peaks, confirming that the superlattices remain attached and do not revert to the initial colloidal state.

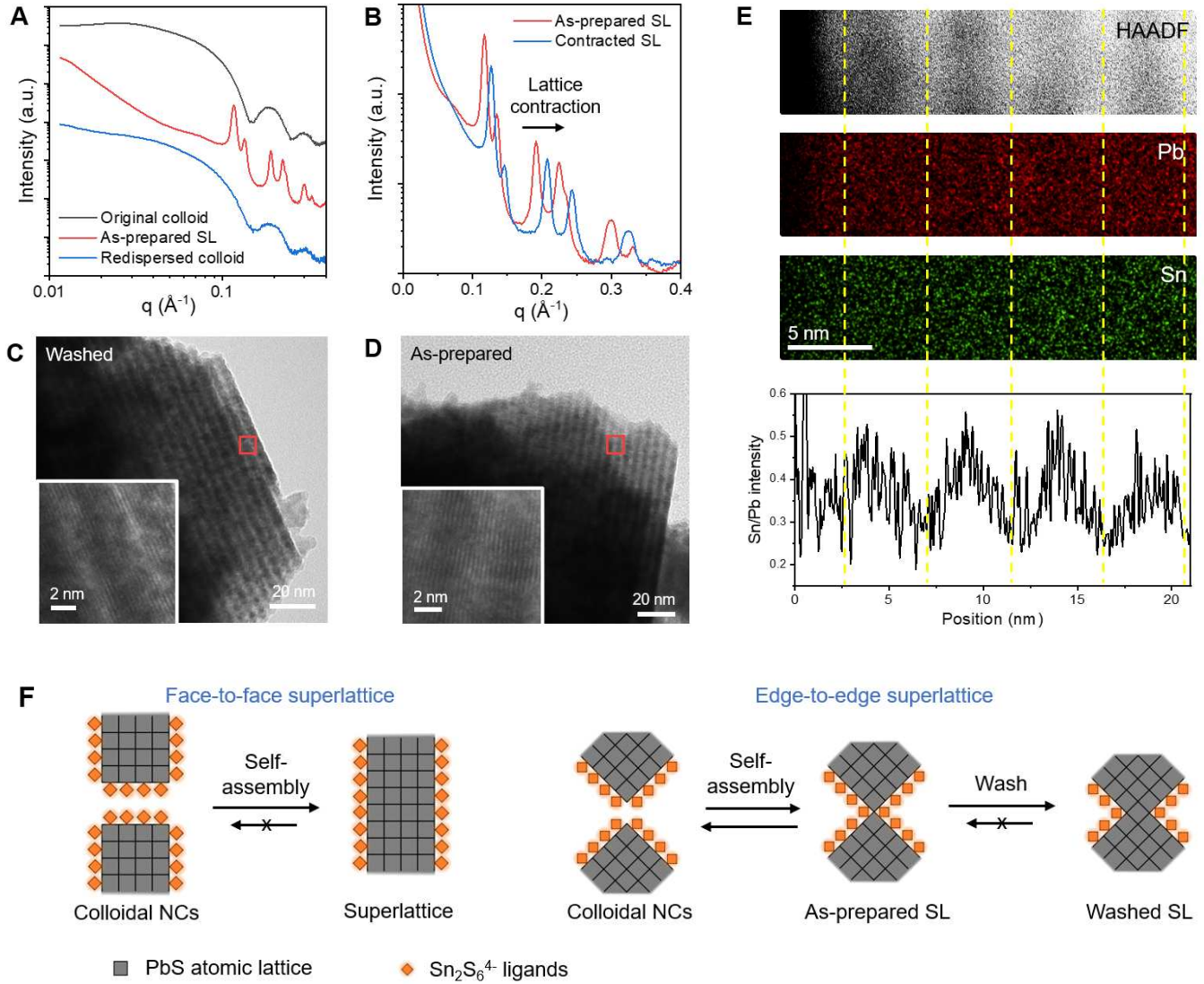


FIG. 5. (A) Small-angle X-ray scattering (SAXS) patterns of the original colloid solution, as-prepared superlattices (SL) and redispersed colloid of $5.7\text{ nm PbS-Sn}_2\text{S}_6^{4-}$ nanocrystals (NCs). The y-axis is vertically offset for clarity. Absence of Bragg peaks from the SAXS pattern of redispersed PbS NCs indicates full disassembly of superlattices. (B) SAXS patterns of as-prepared and washed $5.7\text{ nm PbS-Sn}_2\text{S}_6^{4-}$ NC superlattices. (C, D) Transmission electron microscopy (TEM) images of as-prepared (D) and washed (E) $5.7\text{ nm PbS-Sn}_2\text{S}_6^{4-}$ NC superlattices. Insets: magnified images of the regions highlighted by red squares. (E) HAADF-STEM image and STEM-EDS elemental mapping of the superlattice. The plot below presents the ratio of the Sn and Pb signal counts across the superlattice. (F) Schematic of self-assembly, washing and redispersion processes.

To reconcile these observations, here we discuss the possibility of *reversible* oriented attachment (ROA) and how it may work on the example of $\text{PbS-Sn}_2\text{S}_6^{4-}$ NC superlattices. An important prerequisite for achieving ROA is the minimization of NC contact areas that touch to form a crystalline neck, as large contact areas can make the orientational attachment more prone to defects.⁵⁸⁻⁶¹ Ideally, NCs should approach each other's edge-to-edge to create a line of contact that further grows into a neck (Figures 1D and 5F). Such alignment with low-area contacts is indeed observed in $\text{PbS-Sn}_2\text{S}_6^{4-}$ NC superlattices (Figures 1-3), stabilized by ion layering as described in

the previous Section (Figure 4).

The second requirement for ROA can be related to the chemical nature of inorganic surface ligands. Ideally, such ligands should guide the oriented attachment of NC cores while enabling local rearrangements by delaying formation of irreversible necks between NCs. To study the necks formed between PbS NCs, we carried out STEM-EDS elemental mapping within a $5.9\text{ nm PbS-Sn}_2\text{S}_6^{4-}$ NC superlattice (Figure 5E), along with the corresponding elemental line scan across the superlattice (also see Figure S26). The accumulated EDS spectrum can be found in Figure S27. The bright regions in the HAADF-STEM

image correspond to superlattice planes formed by PbS NCs, while the darker regions represent the interparticle gaps with necks connecting adjacent NCs. The STEM-EDS Pb signal intensity is higher in the brighter regions of the HAADF-STEM image, confirming this correspondence. Notably, the spatial distribution of tin (Sn) exhibits an anti-phase relationship with that of lead (Pb), clearly indicated by the plot of Sn/Pb ratio (Figures 5E and S26). This indicates that the interparticle regions are enriched in Sn, suggesting that the epitaxial bridging of PbS NCs involves $\text{Sn}_2\text{S}_6^{4-}$ surface ligands. Furthermore, the use of K_3AsS_4 as the flocculant can further promote reversibility at an early stage of the oriented attachment because tetrahedrally bonded AsS_4^{3-} ions cannot epitaxially integrate with PbS lattice. We propose that the reversible self-assembly of 5.7 nm PbS- $\text{Sn}_2\text{S}_6^{4-}$ NCs is enabled by the incorporation of excess flocculants (K_3AsS_4) within the superlattice (Figure S28). Washing the superlattice with acetonitrile removes a significant portion of incorporated K_3AsS_4 , as confirmed by the elemental analysis (Table S1). Removal of AsS_4^{3-} triggers the oriented attachment of edge-to-edge oriented PbS- $\text{Sn}_2\text{S}_6^{4-}$ NCs, which is observed as gradual reduction of the lattice constant of *fcc* superlattice (Figures 5B). It is known that $\text{Sn}_2\text{S}_6^{4-}$ ions can dynamically rearrange in polar solvents and may form fragments structurally compatible with PbS cores.^{62,63} The dynamic nature of Sn-S-Sn bonding in polar solvents is expected to favor both oriented attachment of NCs and disassembly of misbonded fragments, gradually leading to the formation of permanent necks between NCs and preventing redispersion of NCs into the colloidal phase.

CONCLUSION

In summary, our results demonstrate that PbS NCs capped with compact and highly charged $\text{Sn}_2\text{S}_6^{4-}$ inorganic ligands can self-assemble into superlattices that exhibit exceptionally high translational and orientational order, approaching single-crystal precision. Structural and compositional analyses reveal that the NCs adopt a distinctive edge-to-edge orientation, promoted by the ionic layering in the electrolyte containing multi-charged ions. We further reveal that the reversibility of this self-assembly is influenced by the incorporation and partial removal of K_3AsS_4 salts during the washing process. The superlattices with incorporated K_3AsS_4 can be completely disassembled into their original colloidal state, whereas the partial removal of salts results in permanent lattice contraction and epitaxial oriented attachment of NCs. These findings highlight the interplay between ligand chemistry, lattice stability, and reversibility, offering a tunable strategy for control of NC assemblies. This ability to reversibly assemble colloidal nanocrystals with atomic-level alignment opens exciting opportunities for

creating dynamic, reconfigurable materials with single-crystal-like properties, holding potential for applications in adaptive optoelectronics, self-healing materials, and nanostructured devices.

METHODS/EXPERIMENTAL

Synthesis of PbS nanocrystals (NCs): The preparations of $\text{Pb}(\text{OA})_2$ and the thiourea precursor were carried out according to the previously reported procedures.³⁴ The synthesis of PbS NCs follows the method adapted from the reported procedures.³⁴

To obtain 5.7 nm PbS-OA NCs, $\text{Pb}(\text{OA})_2$ (5.544 g, 7.2 mmol) and 1-octene (60 mL) were added into a three-neck 250 mL round-bottom flask under a N_2 atmosphere. The mixture was heated to 120 °C in an oil bath while maintaining nitrogen flow, during which $\text{Pb}(\text{OA})_2$ was completely dissolved in the solvent. Separately, N-phenyl-N'-N'-dodecylthiourea (1.923 g, 6 mmol) was mixed with diglyme (2 mL) in a 20 mL vial under nitrogen and sealed with a septum cap. The vial was heated in an oil bath, and after the temperature was stabilized, the thiourea solution was withdrawn using a syringe and swiftly injected into the flask. After 10 min, the reaction was quenched by removing the oil bath and cooling the flask with an air stream. The resulting NCs were transferred into a nitrogen-filled glovebox and precipitated by addition of anhydrous methyl acetate. The NCs were then resuspended in anhydrous hexane and centrifuged to remove insoluble residues. The supernatant was further purified by four cycles of precipitation with methyl acetate and redispersion in hexane. Finally, the washed NCs were redispersed in anhydrous hexane and stored under N_2 .

Ligand exchange: The ligand exchange of PbS NCs follows the previously reported method.³²

Self-assembly: Self-assembled superlattices were prepared by mixing 20 μL of a stock PbS NC solution (50–100 mg/mL) with 40 μL of *N,N*-dimethylformamide (DMF). A 500 mM K_3AsS_4 solution was then added incrementally in 5 μL aliquots at one-minute intervals, with continuous stirring, until a total volume of 40 μL of K_3AsS_4 solution had been added. The mixture was stirred for an additional 20 minutes to form a suspension of superlattice in an NMF/DMF mixture. The resulting suspension was centrifuged for 1 minute, and the supernatant was removed to obtain an "as-prepared" superlattice. To produce a "washed" superlattice, the material was resuspended in approximately 1 mL of acetonitrile (MeCN), centrifuged, and the supernatant was discarded. This washing procedure was repeated twice. The final superlattice samples were then collected and stored.

ACKNOWLEDGEMENTS

We are grateful to Dr. A. Nelson for a critical reading and editing of the manuscript. We thank Progna Banerjee for support for scanning electron transmission microscopy measurements. We thank Dr. Nestor J. Zaluzec for support in STEM-EDS measurements. We thank Dr. X. Zuo for support for X-ray scattering experiments in Advanced Photon Source, Argonne National Laboratory. Materials synthesis and detailed structural characterization of nanocrystal superlattices were supported by the National Science Foundation via the Center for Integration of Modern Optoelectronic Materials on Demand (IMOD) Science and Technology Center under Cooperative Agreement No. DMR-2019444. Simulations were supported by the Office of Basic Energy Sciences (BES), US Department of Energy (DOE) (award no. DE-SC0019375). Self-assembly experiments were supported by the University of Chicago Materials Research Science and Engineering Center, supported by National Science Foundation under award number DMR-2011854. A.J. was partially supported by Kwanjeong Educational Foundation. A.N.S. was supported by a Kavli ENSI Graduate Student Fellowship from the Kavli Nanoscience Institute at UC Berkeley. Y.A.T. was supported by University of Chicago's Quad Undergraduate Research Scholars Program. Work performed at the Center for Nanoscale Materials and Advanced Photon Source, U.S. Department of Energy Office of Science User Facilities, was supported by the U.S. DOE, Office of Basic Energy Sciences, under Contract No. DE-AC02-06CH11357. HAADF-STEM imaging was carried out at the Facility for Electron Microscopy of Materials at the University of Colorado Boulder (CU FEMM, RRID: SCR_019306).

CODE AVAILABILITY

The source code developed for this study, including the field-theoretic Hamiltonian implementation, CUDA-accelerated solvers and the Monte Carlo sampling routines, is available on GitHub at <https://github.com/ansingh1214/Rigid-Field>.

SUPPORTING INFORMATION

Additional figures and tables are provided in the Supporting Information, which includes detailed descriptions of the experimental methods, nanocrystal and nanocrystal film characterization, SAXS, WAXS and SAED analysis, Landau-Ginzburg field theory and numerical simulation details.

- [1] Boles, M.; Engel, M.; Talapin, D. Self-Assembly of Colloidal Nanocrystals: From Intricate Structures to Functional Materials. *Chem. Rev.* **2016**, *116*, 11220–11289.
- [2] Bassani, C. et al. Nanocrystal Assemblies: Current Advances and Open Problems. *ACS Nano* **2024**, *18*, 14791–14840.
- [3] Murray, C.; Kagan, C.; Bawendi, M. Synthesis and Characterization of Monodisperse Nanocrystals and Close-Packed Nanocrystal Assemblies. *Annu. Rev. Mater. Sci.* **2000**, *30*, 545–610.
- [4] Shevchenko, E.; Talapin, D.; Murray, C.; O'Brien, S. Structural Characterization of Self-Assembled Multifunctional Binary Nanoparticle Superlattices. *J. Am. Chem. Soc.* **2006**, *128*, 3620–3637.
- [5] Coropceanu, I.; Boles, M.; Talapin, D. Systematic Mapping of Binary Nanocrystal Superlattices: The Role of Topology in Phase Selection. *J. Am. Chem. Soc.* **2019**, *141*, 5728–5740.
- [6] Talapin, D.; Shevchenko, E.; Bodnarchuk, M.; Ye, X.; Chen, J.; Murray, C. Quasicrystalline Order in Self-Assembled Binary Nanoparticle Superlattices. *Nature* **2009**, *461*, 964–967.
- [7] Rupich, S.; Shevchenko, E.; Bodnarchuk, M.; Lee, B.; Talapin, D. Size-Dependent Multiple Twinning in Nanocrystal Superlattices. *J. Am. Chem. Soc.* **2010**, *132*, 289–296.
- [8] Singh, G.; Chan, H.; Baskin, A.; Gelman, E.; Repnin, N.; Král, P.; Klajn, R. Self-Assembly of Magnetite Nanocubes into Helical Superstructures. *Science* **2014**, *345*, 1149–1153.
- [9] Zhou, S. et al. Chiral Assemblies of Pinwheel Superlattices on Substrates. *Nature* **2022**, *612*, 259–265.
- [10] Rainò, G.; Becker, M.; Bodnarchuk, M.; Mahrt, R.; Kovalenko, M.; Stöferle, T. Superfluorescence from Lead Halide Perovskite Quantum Dot Superlattices. *Nature* **2018**, *563*, 671–675.
- [11] Boles, M.; Talapin, D. Many-Body Effects in Nanocrystal Superlattices: Departure from Sphere Packing Explains Stability of Binary Phases. *J. Am. Chem. Soc.* **2015**, *137*, 4494–4502.
- [12] Overbeek, C.; Peters, J.; Rossum, S.; Smits, M.; Huis, M.; Vanmaekelbergh, D. Interfacial Self-Assembly and Oriented Attachment in the Family of PbX (X = S, Se, Te). *Nanocrystals. J. Phys. Chem. C* **2018**, *122*, 12464–12473.
- [13] Boles, M.; Talapin, D. Binary Assembly of PbS and Au Nanocrystals: Patchy PbS Surface Ligand Coverage Stabilizes the CuAu Superlattice. *ACS Nano* **2019**, *13*, 5375–5384.
- [14] Fundamental Processes and Practical Considerations of Lead Chalcogenide Mesocrystals Formed via Self-Assembly and Directed Attachment of Nanocrystals at a Fluid Interface. *Chem. Mater.* **2021**, *33*, 9457–9472.
- [15] Kim, A. et al. Patchy Nanoparticles by Atomic Stencilling. *Nature* **2025**, *646*, 592–600.
- [16] Tian, Y.; Zhang, Y.; Wang, T.; Xin, H.; Li, H.; Gang, O. Lattice Engineering through Nanoparticle-DNA Frameworks. *Nat. Mater.* **2016**, *15*, 654–661.
- [17] Liu, W.; Halverson, J.; Tian, Y.; Tkachenko, A.; Gang, O. Self-Organized Architectures from Assorted DNA-Framed Nanoparticles. *Nat. Chem.* **2016**, *8*, 867–

873.

[18] Kahn, J.; Gang, O. Designer Nanomaterials through Programmable Assembly. *Angew. Chem.* **2022**, *134*.

[19] Teng, F.; Zhang, H.; Nykypanchuk, D.; Li, R.; Yang, L.; Tiwale, N.; Xi, Z.; Liu, M.; He, M.; Zhang, S.; Gang, O. Macroscale-Area Patterning of Three-Dimensional DNA-Programmable Frameworks. *Nat. Commun.* **2025**, *16*, 3238.

[20] Grzelczak, M.; Liz-Marzán, L.; Klajn, R. Stimuli-Responsive Self-Assembly of Nanoparticles. *Chem. Soc. Rev.* **2019**, *48*, 1342–1361.

[21] Dominguez, M. et al. *D. J. Assembly of Linked Nanocrystal Colloids by Reversible Covalent Bonds. Chem. Mater.* **2020**, *32*, 10235–10245.

[22] Bian, T.; Gardin, A.; Gemen, J.; Houben, L.; Perego, C.; Lee, B.; Elad, N.; Chu, Z.; Pavan, G.; Klajn, R. Electrostatic Co-Assembly of Nanoparticles with Oppositely Charged Small Molecules into Static and Dynamic Superstructures. *Nat. Chem.* **2021**, *13*, 940–949.

[23] Talapin, D.; Murray, C. PbSe Nanocrystal Solids for N- and p-Channel Thin Film Field-Effect Transistors. *Science* **2005**, *310*, 86–89.

[24] Boneschanscher, M.; Evers, W.; Geuchies, J.; Alantzas, T.; Goris, B.; Rabouw, F.; Rossum, S.; Zant, H.; Siebbeles, L.; Tendeloo, G.; Swart, I.; Hilhorst, J.; Petukhov, A.; Bals, S.; Vanmaekelbergh, D. Long-Range Orientation and Atomic Attachment of Nanocrystals in 2D Honeycomb Superlattices. *Science* **2014**, *344*, 1377–1380.

[25] Whitham, K.; Yang, J.; Savitzky, B.; Kourkoutis, L.; Wise, F.; Hanrath, T. Charge Transport and Localization in Atomically Coherent Quantum Dot Solids. *Nat. Mater.* **2016**, *15*, 557–563.

[26] Abelson, A.; Qian, C.; Salk, T.; Luan, Z.; Fu, K.; Zheng, J.-G.; Wardini, J.; Law, M. Collective Topo-Epitaxy in the Self-Assembly of a 3D Quantum Dot Superlattice. *Nat. Mater.* **2020**, *19*, 49–55.

[27] Kovalenko, M.; Scheele, M.; Talapin, D. Colloidal Nanocrystals with Molecular Metal Chalcogenide Surface Ligands. *Science* **2009**, *324*, 1417–1420.

[28] Lee, J.-S.; Kovalenko, M.; Huang, J.; Chung, D.; Talapin, D.-I. T. High Electron Mobility and High Photoconductivity in All-Inorganic Nanocrystal Arrays. *Nat. Nanotechnol.* **2011**, *6*, 348–352.

[29] Jin, H.; Choi, S.; Xing, G.; Lee, J.-H.; Kwon, Y.; Chong, W.; Sum, T.; Jang, H.; Kim, S. SbS43-, and AsS33- Metal Chalcogenide Surface Ligands: Couplings to Quantum Dots, Electron Transfers, and All-Inorganic Multilayered Quantum Dot Sensitized Solar Cells. *J. Am. Chem. Soc.* **2015**, *137*, 13827–13835.

[30] Self-Assembly of Nanocrystals into Strongly Electronically Coupled All-Inorganic Supercrystals. *Science* **2022**, *375*, 1422–1426.

[31] Tanner, C.; Utterback, J.; Portner, J.; Coropceanu, I.; Das, A.; Tassone, C.; Teitelbaum, S.; Limmer, D.; Talapin, D.; Ginsberg, N. In Situ X-Ray Scattering Reveals Coarsening Rates of Superlattices Self-Assembled from Electrostatically Stabilized Metal Nanocrystals Depend Nonmonotonically on Driving Force. *ACS Nano* **2024**.

[32] Jeong, A.; Portner, J.; Tanner, C.; Ondry, J.; Zhou, C.; Mi, Z.; Tazoui, Y.; Lee, B.; Wall, V.; Ginsberg, N.; Talapin, D. Colloidal Dispersions of Sterically and Electrostatically Stabilized PbS Quantum Dots: Structure Factors, Second Virial Coefficients, and Film-Forming Properties. *ACS Nano* **2024**, *18*, 33864–33874.

[33] Tanner, C. et al. Enhancing Nanoscale Charged Colloid Crystallization near a Metastable Liquid Binodal. *Nat. Phys.* **2025**, *21*, 1594–1602.

[34] Hendricks, M.; Campos, M.; Cleveland, G.; Jen-La Plante, I.; Owen, J. A Tunable Library of Substituted Thiourea Precursors to Metal Sulfide Nanocrystals. *Science* **2015**, *348*, 1226–1230.

[35] Fan, Z.; Grünwald, M. Orientational Order in Self-Assembled Nanocrystal Superlattices. *J. Am. Chem. Soc.* **2019**, *141*, 1980–1988.

[36] Weidman, M.; Smilgies, D.-M.; Tisdale, W. Kinetics of the Self-Assembly of Nanocrystal Superlattices Measured by Real-Time in Situ X-Ray Scattering. *Nat. Mater.* **2016**, *15*, 775–781.

[37] Klinger, M. F. More Tools, More CrysTBox. *J. Appl. Crystallogr.* **2017**, *50*, 1226–1234.

[38] Beygi, H.; Sajjadi, S.; Babakhani, A.; Young, J.; Veggel, F. Surface Chemistry of As-Synthesized and Air-Oxidized PbS Quantum Dots. *Appl. Surf. Sci.* **2018**, *457*, 1–10.

[39] Choi, H.; Ko, J.-H.; Kim, Y.-H.; Jeong, S. Steric-Hindrance-Driven Shape Transition in PbS Quantum Dots: Understanding Size-Dependent Stability. *J. Am. Chem. Soc.* **2013**, *135*, 5278–5281.

[40] Zhang, J.; Luo, Z.; Quan, Z.; Wang, Y.; Kumbhar, A.; Smilgies, D.-M.; Fang, J. Low Packing Density Self-Assembled Superstructure of Octahedral Pt3 Ni Nanocrystals. *Nano Lett.* **2011**, *11*, 2912–2918.

[41] Li, D.; Chen, Q.; Chun, J.; Fichthorn, K.; Yoreo, J.; Zheng, H. Nanoparticle Assembly and Oriented Attachment: Correlating Controlling Factors to the Resulting Structures. *Chem. Rev.* **2023**, *123*, 3127–3159.

[42] Zhu, H. et al. Controlling Nanoparticle Orientations in the Self-Assembly of Patchy Quantum Dot-Gold Heterostructural Nanocrystals. *J. Am. Chem. Soc.* **2019**, *141*, 6013–6021.

[43] Hatch, H.; Krekelberg, W.; Hudson, S.; Shen, V. Depletion-Driven Crystallization of Cubic Colloids Sedimented on a Surface. *J. Chem. Phys.* **2016**, *144*, 194902.

[44] Ramasubramani, V.; Vo, T.; Anderson, J.; Glotzer, S. A Mean-Field Approach to Simulating Anisotropic Particles. *J. Chem. Phys.* **2020**, *153*, 084106.

[45] Rosenberg, M.; Dekker, F.; Donaldson, J.; Philipse, A.; Kantorovich, S. Self-Assembly of Charged Colloidal Cubes. *Soft Matter* **2020**, *16*, 4451–4461.

[46] Israelachvili, J. *Intermolecular and Surface Forces*; Academic Press, 2011.

[47] Guerrero García, G.; Cruz, M. Polarization Effects of Dielectric Nanoparticles in Aqueous Charge-Asymmetric Electrolytes. *J. Phys. Chem. B* **2014**, *118*, 8854–8862.

[48] Limmer, D. T. Interfacial Ordering and Accompanying Divergent Capacitance at Ionic Liquid-Metal Interfaces. *Phys. Rev. Lett.* **2015**, *115*, 256102.

[49] Zhang, H.; Dasbiswas, K.; Ludwig, N.; Han, G.; Lee, B.; Vaikuntanathan, S.; Talapin, D. Stable Colloids in Molten Inorganic Salts. *Nature* **2017**, *542*, 328–331.

[50] Kamysbayev, V.; Srivastava, V.; Ludwig, N. B.; Borkiewicz, O. J.; Zhang, H.; Ilavsky, J.; Lee, B.; Chapman, K. W.; Vaikuntanathan, S.; Talapin, D. V. Nanocrystals in molten salts and ionic liquids: experimental observation of ionic correlations extending beyond the Debye length. *ACS nano* **2019**, *13*, 5760–5770.

[51] Bazant, M. Z.; Storey, B. D.; Kornyshev, A. A. Double layer in ionic liquids: Overscreening versus crowding. *Physical review letters* **2011**, *106*, 046102.

[52] Smith, A. M.; Lee, A. A.; Perkin, S. The electrostatic screening length in concentrated electrolytes increases with concentration. *The journal of physical chemistry letters* **2016**, *7*, 2157–2163.

[53] Kornyshev, A. A. Double-layer in ionic liquids: paradigm change? 2007.

[54] Gebbie, M. A.; Valtiner, M.; Banquy, X.; Fox, E. T.; Henderson, W. A.; Israelachvili, J. N. Ionic liquids behave as dilute electrolyte solutions. *Proceedings of the National Academy of Sciences* **2013**, *110*, 9674–9679.

[55] Wuttke, J. Numerically stable form factor of any polygon and polyhedron. *Applied Crystallography* **2021**, *54*, 580–587.

[56] Lee, S.-W.; Mittra, R. Fourier transform of a polygonal shape function and its application in electromagnetics. *IEEE Transactions on Antennas and Propagation* **1983**, *31*, 99–103.

[57] Haxton, T.; Hedges, L.; Whitelam, S. Crystallization and Arrest Mechanisms of Model Colloids. *Soft Matter* **2015**, *11*, 9307–9320.

[58] Ondry, J.; Hauwiller, M.; Alivisatos, A. Dynamics and Removal Pathway of Edge Dislocations in Imperfectly Attached PbTe Nanocrystal Pairs: Toward Design Rules for Oriented Attachment. *ACS Nano* **2018**, *12*, 3178–3189.

[59] Ondry, J.; Philbin, J.; Lostica, M.; Rabani, E.; Alivisatos, A. Resilient Pathways to Atomic Attachment of Quantum Dot Dimers and Artificial Solids from Faceted CdSe Quantum Dot Building Blocks. *ACS Nano* **2019**, *13*, 12322–12344.

[60] Ondry, J.; Philbin, J.; Lostica, M.; Rabani, E.; Alivisatos, A. Colloidal Synthesis Path to 2D Crystalline Quantum Dot Superlattices. *ACS Nano* **2021**, *15*, 2251–2262.

[61] Ondry, J.; Alivisatos, A. Application of Dislocation Theory to Minimize Defects in Artificial Solids Built with Nanocrystal Building Blocks. *Acc. Chem. Res* **2021**, *54*, 1419–1429.

[62] Kovalenko, M.; Bodnarchuk, M.; Zaumseil, J.; Lee, J.-S.; Talapin, D. Expanding the Chemical Versatility of Colloidal Nanocrystals Capped with Molecular Metal Chalcogenide Ligands. *J. Am. Chem. Soc* **2010**, *132*, 10085–10092.

[63] Protesescu, L.; Nachtegaal, M.; Voznyy, O.; Borovinskaya, O.; Rossini, A.; Emsley, L.; Copéret, C.; Günther, D.; Sargent, E.; Kovalenko, M. Atomistic Description of Thiostannate-Capped CdSe Nanocrystals: Retention of Four-Coordinate SnS₄ Motif and Preservation of Cd-Rich Stoichiometry. *J. Am. Chem. Soc* **2015**, *137*, 1862–1874.

Supporting Information for Atomic Alignment in PbS Nanocrystal Superlattices with Compact Inorganic Ligands via Reversible Oriented Attachment of Nanocrystals

Ahhyun Jeong,¹ Aditya N. Singh,² Josh Portner,¹ Xiaoben Zhang,¹ Saghar Rezaie,³ Justin C. Ondry,¹ Zirui Zhou,¹ Junhong Chen,¹ Ye Ji Kim,¹ Richard D. Schaller,^{4,5} Youssef Tazoui,¹ Zehan Mi,¹ Sadegh Yazdi,³ David T. Limmer,^{2,6,7} and Dmitri V. Talapin^{1,4,*}

¹Department of Chemistry, James Franck Institute, and Pritzker School of Molecular Engineering, University of Chicago, Chicago, Illinois 60637, United States

²Department of Chemistry, University of California, Berkeley, California 94720, USA

³Renewable and Sustainable Energy Institute, University of Colorado, Boulder, Colorado, USA

⁴Center for Nanoscale Materials, Argonne National Laboratory, Argonne, Illinois 60439, United States

⁵Department of Chemistry, Northwestern University, Evanston, Illinois, USA

⁶Chemical Sciences and Materials Sciences Divisions, Lawrence Berkeley National Laboratory, Berkeley, California 94720, USA

⁷Kavli Energy NanoSciences Institute, University of California, Berkeley, California 94720, USA

1. MATERIALS

List of precursors: Arsenic (V) sulfide (Santa Cruz Biotechnology, 99.99%), hexyl isothiocyanate (Sigma Aldrich, HPLC grade >98%), lead (II) oxide (Sigma Aldrich, 99.999% trace metal basis), *N*-dodecylamine (Sigma Aldrich, 98%), oleic acid (Fisher Scientific, 99%), oleylamine (Sigma Aldrich, technical grade 70%), phenyl isothiocyanate (Sigma Aldrich, 98%), potassium sulfide (Strem, anhydrous >95%), sodium stannate trihydrate (Sigma Aldrich, 95%), sodium sulfide nonahydrate (Sigma Aldrich, >98%), germanium disulfide (MP Biomedicals), tin (II) selenide (99.995%, Sigma-Aldrich), trifluoroacetic acid (Fisher Scientific, >99% for spectroscopy), trifluoroacetic anhydride (Sigma Aldrich, 99%), and triethylamine (Sigma Aldrich, >99.5%) were used as received.

List of solvents: Acetone (Fisher Scientific, >99.5%), acetonitrile (Sigma Aldrich, anhydrous 99.8%), diethylene glycol dimethyl ether (Sigma Aldrich, anhydrous 99.5%), dimethylsulfoxide (Sigma Aldrich, >99.9%), hexanes (Fisher Scientific, >98.5%), 1-octadecene (Sigma Aldrich, technical grade 90%), 1-octene (Sigma Aldrich, for synthesis >97%), 2-isopropanol (Fisher Scientific, >99.5%), methanol (Fisher Scientific, >99.9%), ethanol (>99.5%, anhydrous, 200 proof), methyl acetate (Sigma Aldrich, anhydrous 99.5%), *N,N*-dimethylformamide (Sigma Aldrich, anhydrous 99.8%), *N*-methylformamide (Sigma Aldrich, 99%), *N*-methylpropionamide (Sigma Aldrich, 98%), *n*-hexane (Sigma Aldrich, anhydrous 95%), and toluene (Fisher Scientific, >99.8%) were used as received.

2. SAMPLE PREPARATION

Synthesis of PbS nanocrystals (NCs): Synthesis of oleate-capped PbS (PbS-OA) NCs follows a previously reported procedure, including the preparations of Pb(OA)₂ and the thiourea precursor.

To obtain 5.7 nm PbS-OA NCs, Pb(OA)₂ (5.544 g, 7.2 mmol) and 1-octene (60 mL) were added into a three-neck 250 mL round-bottom flask under a N₂ atmosphere. The mixture was heated to 120 °C in an oil bath while maintaining nitrogen flow, during which Pb(OA)₂ was completely dissolved in the solvent. Separately, N-phenyl-*N'*-*N*'-dodecylthiourea (1.923 g, 6 mmol) was mixed with diglyme (2 mL) in a 20 mL vial under nitrogen and sealed with a septum cap. The vial was heated in an oil bath, and after the temperature was stabilized, the thiourea solution was withdrawn using a syringe and swiftly injected into the flask. After 10 min, the reaction was quenched by removing the

* Corresponding author: dvtalapin@uchicago.edu

oil bath and cooling the flask with an air stream. The resulting NCs were transferred into a nitrogen-filled glovebox and precipitated by the addition of anhydrous methyl acetate. The NCs were then resuspended in anhydrous hexane and centrifuged to remove insoluble residues. The supernatant was further purified by four cycles of precipitation with methyl acetate and redispersion in hexane. Finally, the washed NCs were redispersed in anhydrous hexane and stored under N₂.

Size-control of PbS-OA NCs was carried out by tuning the thiourea precursor, temperature and solvents. To obtain 5 nm PbS-OA NCs, similar procedure was used, except a solution of *N*-(*p*-(trifluoromethyl)phenyl)-*N'*-dodecylthiourea (2.331 g, 6 mmol) in 2 ml of diglyme was injected into a solution of Pb(OA)₂ (5.544 g, 7.2 mmol) and 1-octene (60 mL) at 120 °C. To obtain 7.3 nm PbS-OA NCs, a solution of *N*-phenyl-*N'*-*N'*-dodecylthiourea (1.923 g, 6 mmol) in 2 ml of diglyme was injected into a solution of Pb(OA)₂ (5.544 g, 7.2 mmol) in 1-octadecene (60 mL) at 120 °C. To obtain 8.3 nm PbS-OA NCs, a solution of *N*-*N*-hexyl-*N'*-dodecylthiourea (1.972, 6 mmol) in 2 ml of diglyme was injected to a solution of Pb(OA)₂ (5.544 g, 7.2 mmol) in 1-octadecene (60 mL) at 150 °C. The same washing procedure was adopted across various PbS-OA NCs.

Preparation of inorganic salt The preparation of 200 mM K₄Sn₂S₆, 500 mM K₃AsS₄ and 200 mM K₄Sn₂Se₆ solutions in *N*-methylformamide (NMF) follows the previously reported method.^{1,2} A 500 mM K₄GeS₄ solution in NMF was prepared by dissolving a stoichiometric ratio of anhydrous K₂S and GeS₂ in distilled NMF and stirring overnight. Undissolved solids were removed by centrifugation.

Ligand exchange: The ligand exchange of PbS NCs follows previously reported method.³

Self-assembly: Self-assembled superlattices were prepared by mixing 20 μL of a stock PbS NC solution (50–100 mg/mL) with 40 μL of *N,N*-dimethylformamide (DMF). A 500 mM K₃AsS₄ solution was then added incrementally in 5 μL aliquots at one-minute intervals, with continuous stirring, until a total volume of 40 μL of K₃AsS₄ solution had been added. The mixture was stirred for an additional 20 minutes to form a suspension of superlattice in an NMF/DMF mixture. The resulting suspension was centrifuged for 1 minute, and the supernatant was removed to obtain an "as-prepared" superlattice. To produce a "washed" superlattice, the material was resuspended in approximately 1 mL of acetonitrile (MeCN), centrifuged, and the supernatant was discarded. This washing procedure was repeated twice. The final superlattice samples were then collected and stored.

Characterization methods

SAXS: Small-angle X-ray scattering (SAXS) collected using a SAXSLAB Ganesha Instrument with a Cu K-alpha source. Colloidal QDs were characterized in glass capillaries that were flame-sealed in air. Superlattices were suspended in a small volume of MeCN (~20 μL) and were drop-cast on Kapton tape. The MeCN was allowed to evaporate under vacuum before the measurement.

TEM: Transmission electron microscopy (TEM) images were acquired using an FEI Tecnai G2 F30 X-TWIN operating at an accelerating voltage of 300 kV. Superlattice samples were prepared by suspending the superlattices in approximately 500 μL of MeCN and drop-casting the suspension onto 400-mesh copper grids with an amorphous carbon support film (Ted Pella). The MeCN was allowed to evaporate in air prior to imaging. Dispersed nanocrystal (NC) samples were prepared by drop-casting a dilute solution of colloidal NCs in NMF onto 400-mesh copper grids with an amorphous carbon support (Ted Pella) that had been treated with oxygen plasma (Harrick Plasma Cleaner, PDC-001) for 10 seconds. The NMF was evaporated under vacuum before imaging.

TEM-SAED: Transmission electron microscopy selected area electron diffraction (TEM-SAED) images were collected using FEI Tecnai G2 F30 X-TWIN at an accelerating voltage of 300 kV. The method for sample preparation was identical to TEM.

STEM-EDS: STEM-EDS mapping were conducted under 300 kV using the Analytical PicoProbe Electron Optical Beam Line, a prototype of the ThermoFisher Spectra UltraX Illiad located at Argonne National Laboratory. Microanalysis measurements of the elemental distribution were obtained using the X-ray Perimeter Array Detector (XPAD) with a capability over 4.5 sR was equipped, guaranteeing the ultrahigh sensitivity for elemental analysis.⁴ For elemental mapping shown in Figure 5E, Pb-L lines and Sn-L lines were used to map Pb and Sn, respectively.

HAADF-STEM: High-angle annular dark field scanning transmission electron microscopy (HAADF-STEM) images were acquired in an aberration-corrected Thermo Fisher Scientific (TFS) Titan Themis operated at an accelerating voltage of 300 kV. The imaging was performed with the convergence semi-angle of 25 mrad, a HAADF detector collection angle range of 52–200 mrad, a beam current of 41 pA, and a dwell time of 2 μsec per pixel. Samples were prepared by depositing dry powder on TEM grids (Ted Pella, Prod#01824; ultrathin carbon film on lacey carbon support film, 400 mesh, Cu). A TFS low background double-tilt TEM holder was used to tilt superlattices along the

desired zone-axis.

3. ANALYSIS METHODS

3.1. Size distribution

The size distribution of $\text{PbS-Sn}_2\text{S}_6^{4-}$ NCs was determined from SAXS analysis of the corresponding NCs capped with oleic acid ligands. Direct extraction of size distribution from the SAXS patterns of $\text{PbS-Sn}_2\text{S}_6^{4-}$ NCs was avoided because the $\text{Sn}_2\text{S}_6^{4-}$ ligands consist of relatively heavy elements compared to the solvent environment, scattering the X-ray and leading to an overestimation of NC diameter. The size distribution was obtained in IgorPro9 using the maximum entropy method via the Irena tool. The resulting number-weighted size distributions were fitted with Gaussian functions to extract mean diameters and standard deviations.

3.2. Scherrer analysis of SAED patterns

In this section, the selected area electron diffraction (SAED) pattern shown in the inset of Figure 2A was analyzed to estimate the Scherrer diameter of the $\text{PbS-Sn}_2\text{S}_6^{4-}$ NC superlattice. Owing to the orientational alignment of the superlattice, an extension of Scherrer analysis to the assembled structure was anticipated. The center of the diffraction pattern was first determined using the DiffTools plugin in Gatan DigitalMicrograph software. A linear intensity profile passing through the center of the pattern (Figure S12A) was then extracted to identify diffraction peaks. Scherrer analysis was performed on the sharpest peak in the linear profile, as indicated in Figure S12B.

The Scherrer diameter (D) is calculated from the full-width half-maximum (FWHM) of the selected peak. The classical Scherrer equation is given by:

$$D = \frac{K\lambda}{\beta \cos(\theta)} \quad (4.1)$$

Where K is the shape factor, λ is wavelength of the incident beam, β is the FWHM of scattering angle in radians and θ is the Bragg angle.⁵ Since our measurement is in reciprocal space in $1/d$ scale rather than in angular space, a modified form of the equation was employed, where Δq is the FWHM in the reciprocal space. The shape factor, K , can be estimated as 0.93 for spherical particles.

$$D = \frac{K}{\Delta q} \quad (4.2)$$

From this analysis, a Scherrer diameter of 6.1 nm was obtained for the $\text{PbS-Sn}_2\text{S}_6^{4-}$ NC superlattice. This value is larger than the estimated diameter of individual $\text{PbS-Sn}_2\text{S}_6^{4-}$ NCs derived from powder X-ray diffraction shown in Figure S13 (PXRD) (5.4 nm). The increase in Scherrer diameter upon self-assembly supports the presence of oriented attachment of NCs within the superlattice. The relatively small Scherrer diameter compared to the estimated superlattice size (on the order of microns) may be attributed to instrumental broadening, e-beam convergence, and to the emergence of satellite peaks due to the periodic superlattice structure.⁶ To confirm this, the diffraction patterns of superlattices were modelled.

The Debye equation can be used to model the diffraction pattern of an ensemble of identical randomly oriented particles. N atoms in each particle will have its coordinates: r_1, r_2, \dots, r_N and atomic form factor (structural amplitude) f_1, f_2, \dots, f_N . The amplitude of scattering is equal to the sum of scattering amplitudes of each individual atom:

$$F(\theta) = \sum_j^N f_j(\theta) e^{\frac{2\pi i}{\lambda} (\mathbf{s} - \mathbf{s}_0, \mathbf{r}_j)} \quad (4.3)$$

Given that the intensity of scattering is $I(\theta) = F(\theta) \cdot F^*(\theta)$:

$$I(\theta) = \sum_m \sum_n f_m(\theta) f_n(\theta) \exp\left(\frac{2\pi i}{\lambda}(\mathbf{s} - \mathbf{s}_0, \mathbf{r}_{mn})\right) \quad (4.4)$$

By integrating the wave vector in different directions, the intensity can be expressed as follows:

$$\overline{I(\theta)} = \sum_m \sum_n f_m(\theta) f_n(\theta) \frac{\sin(2\pi S r_{mn})^*}{2\pi S r_{mn}} \quad (4.5)$$

The angle-dependent atomic form factor in equation is calculated by Hartree-Fock wavefunctions by Cromer and Mann:

$$f_m(\theta) = \exp\left(-B \sin^2 \theta / \lambda^2\right) \left[\sum_{i=1}^4 a_i \exp\left(-\frac{b_i \sin^2 \theta}{\lambda^2}\right) + c \right] \quad (4.6)$$

where λ is wavelength of x-ray, B is Debye-Waller factor which is correlated with thermal vibrations of the atoms, a_i , b_i & c are numerical fitting factors.⁷

The lattice parameters of the simulated PbS-Sn₂S₆⁴⁻ NC superlattices were derived from experimental PXRD and SAXS data. Scherrer analysis of the PXRD pattern (Figure S16) yielded NC dimensions of 5.0 nm along the [100] direction and 4.6 nm along [111] direction. SAXS analysis of the corresponding superlattice (Figure 5B, blue line) indicated a lattice constant of 8.4 nm. These values suggest that the edges of neighboring NCs are atomically precisely aligned, consistent with the oriented order that were observed. The illustration of the model is shown in Figure S17.

The diffraction pattern of the PbS-Sn₂S₆⁴⁻ NC superlattice was simulated using the Debye equation, applied to a single face-centered cubic (fcc) unit cell. Figure S18 shows simulated scattering patterns for NCs with dimensions of 5.0 nm along the [100] direction and 4.6 nm along [111], with lattice constants ranging from 8.4 nm to 20 nm. Compared to the single-particle model, the simulated pattern for a lattice constant of 8.4 nm exhibits significantly sharper peaks, indicating enhanced structural coherence. As the lattice constant increases from 8.4 nm to 8.7 nm, the {111} peak broadens and begins to split. At larger lattice constants, this peak splitting becomes less pronounced, and no noticeable broadening is observed at 20 nm.

To validate the use of a single unit cell as a simulation model, the effect of repeating units on the scattering pattern was examined. Figure S19 shows simulated scattering patterns for one monolayer, one unit cell, and two unit cells of the superlattice. The absence of significant differences among the patterns supports the use of a single unit cell in the simulations.

In summary, simulations of the PbS-Sn₂S₆⁴⁻ NC superlattice confirm that self-assembly should lead to peak sharpening in the SAED pattern, consistent with predictions from the Scherrer equation. However, the emergence of satellite peaks in the superlattice may limit the extent of peak sharpening.

3.3. Wulff construction ratio from PXRD

The Wulff construction ratio $h(111)/h(100)$ for 5.7 nm PbS-Sn₂S₆⁴⁻ NCs was determined from the Scherrer size of the (111) and (200) peaks in the PXRD pattern (Figure S6), calculated using SmartLab Studio II (Rigaku). The Scherrer sizes were 55.7 Å and 54.4 Å, respectively, yielding a Wulff ratio of 1.02.

4. FIELD-THEORETIC SIMULATIONS

4.1. Field theory for strong electrolytes

(A) Expression for the Hamiltonian. The theoretical framework employed is a phenomenological Landau-Ginzburg field theory, adapted for describing strongly correlated ionic systems. The order parameter is the local

charge density, defined as $\phi(\mathbf{r}) = (\phi_+(\mathbf{r}) - \phi_-(\mathbf{r}))/\phi$, where $\phi_+(\mathbf{r})$ and $\phi_-(\mathbf{r})$ are the densities of cationic and anionic species weighted by their valency, respectively, and ϕ is the bulk density. This order parameter, $\phi(\mathbf{r})$, captures local deviations from charge neutrality and its spatial fluctuations dictate the system's structural correlations. The effective Hamiltonian, or free energy functional, for this order parameter is given by

$$\mathcal{H}[\{\phi(\mathbf{r})\}] = -a \int d\mathbf{r} \phi^2(\mathbf{r}) + m \int d\mathbf{r} |\nabla \phi(\mathbf{r})|^2 + Q^2 \int \int d\mathbf{r} d\mathbf{r}' \frac{\phi(\mathbf{r}) \phi(\mathbf{r}')}{|\mathbf{r} - \mathbf{r}'|} \quad (5.1)$$

which incorporates three key contributions governing the behavior of the electrolyte. The first two terms $-a \int d\mathbf{r} \phi^2(\mathbf{r})$ and $m \int d\mathbf{r} |\nabla \phi(\mathbf{r})|^2$, with phenomenological parameter $a, m > 0$, represent the local free energy cost associated with slow spatial variations in the charge density, reflecting energetic costs associated with interfacial tension and other entropic interactions that have correlations spanning short distances, typically spanning the molecular diameter of the electrolyte.⁸ The final term, $Q^2 \int \int d\mathbf{r} d\mathbf{r}' \frac{\phi(\mathbf{r}) \phi(\mathbf{r}')}{|\mathbf{r} - \mathbf{r}'|}$, accounts for the long-range Coulomb interactions between charge density fluctuations, where the coupling strength $Q^2 = q^2/(4\pi\epsilon_0\epsilon)$ depends on the ionic charge q and the solvent's relative dielectric constant ϵ . Higher-order terms in the order parameter expansion, are neglected, which is a valid approximation assuming the system is studied above any bulk ordering temperature, such that the harmonic description captures the essential fluctuations around the disordered bulk liquid state. Consistent with the motivation provided earlier, this Hamiltonian focuses on the interplay between short-range correlations and electrostatics; explicit van der Waals contributions are neglected in this analysis as the specific orientational ordering is expected to be primarily dictated by the longer-range forces that emerge from the anisotropic interactions of the interfaces with the induced charge layering.

For analytical and computational convenience, the Hamiltonian is often expressed in Fourier space:

$$\hat{\mathcal{H}}[\{\phi(\mathbf{k})\}] = \frac{1}{16\pi^3} \int d\mathbf{k} \hat{\chi}^{-1}(k) \left| \hat{\phi}(\mathbf{k}) \right|^2 \quad (5.2)$$

with susceptibility

$$\hat{\chi}(k) = \left(-2a + 2mk^2 + \frac{8Q^2}{k^2} \right)^{-1} = \left[2a \left(l_c^2 k^2 + \frac{1}{l_s^2 k^2} - 1 \right) \right]^{-1} \quad (5.3)$$

where we note that phenomenological parameters a, m and Q can be related to physical length scales. In the long-wavelength limit ($k \rightarrow 0$), the Coulomb term dominates, defining the Debye screening length $l_s = \sqrt{a/(4\pi Q^2)}$ which characterizes the exponential decay of correlations in the mean-field limit. In the short-wavelength limit $k \rightarrow \infty$, the gradient term dominates, defining a bare correlation length $l_c = \sqrt{m/a}$, representing the intrinsic length scale of short-range, non-electrostatic correlations. The competition between these two length scales, l_c and l_s , dictates the nature of charge correlations and screening in the system.

(B) Susceptibility in real space.

To understand the spatial structure of charge correlations predicted by this model, we derive the real-space susceptibility, $\chi(r)$, that describes the charge density response at position r due to a point charge perturbation at the origin. This function can be computed by performing an inverse Fourier transform on $\hat{\chi}(k)$ defined in Equation 5.3. We are interested in a bulk theory that describes local order but not long-range order,⁹⁻¹¹ which corresponds to the regime $l_s/l_c < 2$. Using the residue theory, the real-space susceptibility $\chi(r)$ characterized by damped oscillations, takes the form:

$$\chi(r) = A \exp(-r/\alpha) \cos(\gamma r/\alpha - \theta) / (4\pi r) \quad (5.4)$$

Here, the parameters α and γ govern the decay and oscillation characteristics, respectively, while θ is a phase shift and A is the amplitude. All these quantities are related to the fundamental length scales l_c and l_s by:

$$\alpha = 2l_c l_s^{1/2} (2l_c - l_s)^{-1/2}, \quad \gamma = \sqrt{\frac{2 + l_s/l_c}{2 - l_s/l_c}}, \quad \theta = \sin^{-1}(l_s/2l_c), \quad A = \frac{1}{al_c \sqrt{4l_c^2 - l_s^2}} \quad (5.5)$$

This oscillatory form of $\chi(r)$ mathematically represents the phenomenon of charge layering where correlations decay with distance r via an envelope function $e^{-r/\alpha}$ while oscillating with a characteristic wavelength given by $2\pi\alpha/\gamma$. A visualization of this oscillatory behavior and the influence of α and γ is presented in Figure S18A and S18B, which plots $4\pi r A^{-1} \chi(r)$ to emphasize the structural oscillations over the $1/r$ geometric decay. This susceptibility forms the basis for understanding the effective interactions between the NCs mediated by the electrolytes.

4.2. Inclusion of Rigid body constraints

To simulate the system in this work, the field theory described above must be extended to incorporate the Pb NCs. We introduce terms to the Hamiltonian representing the rigid NC bodies and their coupling to the ionic environment mediated through the charged MCC ligands that are grafted to the surface.

(A) Expression for the modified Hamiltonian. We assume that the system comprises N NCs and denote \mathbf{r}_j and \mathbf{R}_j as the position and orientation (expressed through the rotation matrix) of the j^{th} NC respectively. The coupling between the NC and the field theory is introduced through two additional terms representing key physical effects: (i) the asymmetric charge density inside the nanocrystal is zero, that is imposed through a quadratic penalty with Lagrange multiplier λ :

$$\lambda \sum_j^N \int_{\Omega_j} d\mathbf{r} |\phi(\mathbf{r})|^2 \quad (5.6)$$

where \int_{Ω_j} denotes the volume integral over the j^{th} NC, and (ii) the interface of the nanocrystal attracts negative charges, that is imposed through a linear term:

$$b \sum_j^N \int_{\partial\Omega_j} d\mathbf{r} \phi(\mathbf{r}) \quad (5.7)$$

where $\int_{\partial\Omega_j}$ denotes the surface integral over the j^{th} NC and $b > 0$ modulates the interaction strength. With the inclusion of these two terms, the Hamiltonian in fourier space takes the form:

$$\begin{aligned} \mathcal{H}[\{\phi(\mathbf{k})\}; \{\mathbf{r}_j\}, \{\mathbf{R}_j\}] = & \frac{1}{16\pi^3} \int d\mathbf{k} \hat{\chi}^{-1}(\mathbf{k}) |\hat{\phi}(\mathbf{k})|^2 + \frac{\lambda}{64\pi^6} \iint d\mathbf{k}' d\mathbf{k} \hat{\phi}(\mathbf{k}) \hat{\phi}(\mathbf{k}') \sum_j^N \hat{\eta}_j(-\mathbf{k} - \mathbf{k}'; \mathbf{r}_j, \mathbf{R}_j) \\ & + \frac{b}{8\pi^3} \int d\mathbf{k} \hat{\phi}(\mathbf{k}) \sum_j^N \hat{\Sigma}_j(-\mathbf{k}; \mathbf{r}_j, \mathbf{R}_j) \end{aligned} \quad (5.8)$$

where $\hat{\chi}(\mathbf{k})$ is the inverse of the susceptibility in Fourier space defined in Equation 5.3 and $\hat{\eta}_j(\mathbf{k})$ and $\hat{\Sigma}_j(\mathbf{k})$ is the volume and surface form-factor of the j^{th} NC respectively, computed via the fourier transform of the volume and surface integrals defined in Equation 5.6 and 5.7 respectively. By taking the functional derivative of the Hamiltonian, the corresponding Euler-Lagrange equation for fixed positions and orientations of the NCs is given by

$$\hat{\chi}^{-1}(\mathbf{k}) \hat{\phi}(\mathbf{k}) + \sum_j^N \frac{\lambda}{4\pi^3} [\hat{\phi} \circledast \hat{\eta}_j](\mathbf{k}) = - \sum_j^N b \hat{\Sigma}_j(\mathbf{k}) \quad (5.9)$$

where \circledast denotes the convolution operator, and net neutrality is imposed by disregarding the $k = 0$ term. While the Euler-Lagrange equations can be solved through a linear solver to get the free-energies, the accuracy of numerical calculations strongly resides in the resolution of the interface and the volume form factors. The Hamiltonian is highly sensitive to the form factors, resulting in strong artifacts for different orientations when standard interpolation-based methods are used. To resolve this issue, we derive analytical equations for the form factors of truncated octahedra.

(B) Interpolation free representation using analytical form factors. Accurately representing the truncated octahedral NC geometry within the Fourier space Hamiltonian (Equation 5.8) and the corresponding Euler-Lagrange

equation (Equation 5.9) requires computation of the volume and surface form factors, $\hat{\eta}_j(\mathbf{k})$ and $\hat{\Sigma}_j(\mathbf{k})$. Direct calculation of these factors on a discrete grid can introduce interpolation artifacts, particularly when representing arbitrarily oriented NCs that are not aligned with the grid's axes. To overcome this, we employ analytical expressions for the form factors derived from the NC's geometry.

The surface of the truncated octahedron is composed of 6 square faces and 8 hexagonal faces. The total surface form factor $\hat{\Sigma}_j(\mathbf{k})$ for an NC indexed by j centered at the origin is computed by summing the analytical Fourier transforms of each of its individual faces l , denoted $\hat{\Sigma}_{jl}(\mathbf{k})$:

$$\hat{\Sigma}_j(\mathbf{k}) = \sum_{l \in \partial\Omega_j} \hat{\Sigma}_{jl}(\mathbf{k}) \hat{G}(\mathbf{k}) \quad (5.10)$$

The specific analytical form of $\hat{\Sigma}_{jl}(\mathbf{k})$ can be obtained analytically for both squares and hexagons^{12,13} and depend on the distance from the center of the face from the origin and the relative orientation of the face with respect to the grid's principal axis. $\hat{G}(\mathbf{k})$ is a Gaussian smearing function, defined as:

$$\hat{G}(\mathbf{k}) = \exp\left(-\sigma^2 |\mathbf{k}|^2 / 2\right) \quad (5.11)$$

where $\sigma = 2\text{\AA}$ is the standard deviation in real space chosen to avoid numerical instabilities due to Gibbs oscillations. All these terms are calculated by first computing the relative distance to the truncated octahedra's center and the relative orientation of the faces with respect to the principal axis of the truncated octahedra, and then by computing the relative position \mathbf{r}_j and orientation \mathbf{R}_j of the j^{th} octahedra with respect to the grid.

The volume form factor, $\hat{\eta}_j(\mathbf{k})$, is obtained from the surface form factors using the divergence theorem:¹²

$$\hat{\eta}_j(k) = \frac{i}{|\mathbf{k}|^2} \sum_{l \in \partial\Omega_j} (\mathbf{k} \cdot \hat{\mathbf{n}}_{jl}) \hat{\Sigma}_{jl}(\mathbf{k}) \hat{G}(\mathbf{k}) \quad (5.12)$$

where $\hat{\mathbf{n}}_{jl}$ is the outward unit normal vector of face l , that depends on the position and orientation of the NC. For $\mathbf{k} = 0$, $\hat{\eta}_j(0)$ corresponds to the volume of the truncated octahedron. This analytical, interpolation-free approach allows for accurate and efficient evaluation of the rigid body constraints for any NC position and orientation within the simulation framework.

4.3. Computational methods

To explore the thermodynamic landscape governed by the Hamiltonian, our computational approach involves the minimization of the charge density field and the sampling of nanoparticle configurations.

(A) Minimization of charge density field. For a given configuration of nanocrystals, defined by their positions $\{\mathbf{r}_j\}$ and orientations $\{\mathbf{R}_j\}$, the equilibrium charge density field $\hat{\phi}(\mathbf{k})$ is determined by numerically solving the Euler-Lagrange equation in Equation 5.9. The system is discretized onto a periodic cubic grid, with a box size L corresponding to the desired physical dimensions. The grid spacing $dx = L/N_g$ is chosen to be approximately $0.8\text{\AA} - 1\text{\AA}$, which is more than sufficient to converge free energy estimates up to 0.01% for the smallest wavevector chosen.

We solve the Euler-Lagrange equation, Equation 5.9, efficiently in Fourier space, which allows for the straightforward application of the analytical form factors described previously and the use of Fast Fourier Transforms (FFTs) for evaluating convolution terms. We employ the CUDA accelerated matrix free Conjugate Gradient (CG) algorithm implemented in CuPy to solve the resulting linear set of equations. To accelerate convergence, a preconditioner based on the Fourier space susceptibility, $\hat{\chi}(\mathbf{k})$, is applied during the CG iterations. The linear operator within the CG method incorporates the inverse susceptibility $\hat{\chi}^{-1}(\mathbf{k})$ and the volume constraint term, which involves the convolution $[\hat{\phi} \otimes \hat{\eta}_j](\mathbf{k})$ implemented via FFTs.

The iterative process continues until the residual norm falls below a specified tolerance threshold, set to 10^{-6} for all calculations. The resulting field $\hat{\phi}^*(\mathbf{k})$ represents the equilibrium charge density distribution for the specified nanocrystal arrangement and is subsequently used for calculating the system's free energy at a fixed position and orientation of the NCs. The code for the field theory implementation is available online.

(B) Free energy computation for 2 nanocrystals. To characterize the effective interaction potential between a pair of NCs mediated by the strong electrolytes, we performed calculations using the field theory described above. The system consisted of two truncated octahedral NCs, each with a diameter of 57 Å, placed within a cubic simulation box of side length $L = 200$ Å, discretized onto a $200 \times 200 \times 200$ grid. For the field parameters, we used $\alpha = 3.0$ Å and $\gamma = 2.1$, which allows us to uniquely define the physical length scales l_c and l_s . The amplitude of the density waves is dictated by the ratio between the strength of the source term at the interface b to the harmonic term a in the Hamiltonian. For all simulations, we use $b/a = 100$ Å. Additionally, the magnitude of the Lagrange multiplier is chosen to be $\lambda/a = 500$, which is sufficient to prevent charge penetration into the volume of the NC up to 2–4% of the maximum density observed. The energy scale is set by defining the reduced temperature $k_B T = 1$, and the strength of the source term $b/k_B T = 100$ Å⁻².

For this two-particle system, the center-to-center separation distance, r , was systematically varied between 62 Å to 95 Å. At each separation distance, the free energy of the system was computed for different relative orientations of the NCs, focusing specifically on comparing configurations where the NCs were aligned versus non-aligned. The equilibrium charge density field $\hat{\phi}^*(\mathbf{k})$ for each specific configuration (separation r , relative orientation $\mathbf{R}_1, \mathbf{R}_2$) was obtained using the preconditioned CG solver. The total free energy for both orientation was then calculated from this field, summing the relevant contributions (harmonic, gradient, Coulomb, interface, and constraint terms) and subtracting it from the total free energy at the largest distance of separation for the aligned case. At the largest distance of separation considered, the absolute free energy difference between the aligned and nonaligned system was found $0.003 k_B T$, < 0.02% of the free energy difference between the free energy at the minima of the aligned state, correctly reflecting the physical result that the Hamiltonian of non-interacting NCs is invariant to the orientation of the NC.

(C) Phase diagram for orientational order. To determine the thermodynamically preferred orientational phases of the NCs within an FCC superlattice structure, we performed Monte Carlo (MC) simulations as a function of the electrolyte screening parameters α and reduced wavevector γ . The simulations modeled a system of four truncated octahedral NCs placed on the sites of a single FCC unit cell with lattice constant 90 Å. The parameter space scanned covered α from 1.8 Å to 4.0 Å in steps of 0.1 Å and γ from 1.1 to 4.0 in steps of 0.1. The grid size N_g was chosen between 100 to 120, depending on the value of γ/α that sets the Nyquist limit. As before, the relative strength of the source term and the Lagrange multiplier is set through the ratios $b/a = 100$ Å and $\lambda/a = 500$. Finally, the energy scale is set through the reduced temperature, $k_B T = 50$ and the magnitude of the source term $b/k_B T = 2$ Å⁻², chosen to allow for efficient sampling of the system in a regime where thermodynamics governing the orientational order is driven by the free energetics of charge layering, while enabling efficient sampling of the phase space without getting stuck in trapped states.

For each (α, γ) pair, an independent MC simulation was performed to sample the orientational configurations of the four NCs, where the initial orientations were drawn from the Haar distribution. At each MC step, a single NC with index j was chosen at random, and its orientation matrix \mathbf{R}_j was perturbed to generate a trial orientation \mathbf{R}'_j . This rotational move was implemented by generating a 3×3 skew-symmetric matrix \mathbf{W} from a random 3D vector drawn from an isotropic Gaussian distribution with standard deviation $\epsilon = 0.2$, and then applying the rotation $\mathbf{R}'_j = e^{\mathbf{W}} \mathbf{R}_j$. Each simulation consisted of 40,000 such rotational MC steps. The trial move was accepted based on the standard Metropolis criterion using the change in total free energy, ΔF , calculated via the field theory solver. The acceptance rate was found to be 0.3 at the start of the simulation and decreased to < 0.1 as the system approached an orientationally ordered state.

To quantify the degree of alignment, we defined a single-particle order parameter, s_j , for the j^{th} NC based on its orientation matrix R_j relative to the simulation box axes

$$s_j = \left(\sum_{l=1}^3 \max_{m=1,2,3} |(\mathbf{R}_j)_{lm}| \right) - 2 \quad (5.13)$$

This parameter measures the alignment of the NC's primary axes (represented by the columns of R_j) with the Cartesian axes of the simulation frame, accounting for all possible symmetry elements of the octahedral group O_h . The average order parameter for the system, $\langle s \rangle = (1/N) \sum_{j=1}^N s_j$, was calculated at each MC step. After discarding the initial portion of the trajectory for equilibration, the equilibrium value $\langle s \rangle$ for each (α, γ) point was obtained by averaging s over the final 10,000 MC steps.

The orientational phase diagram (presented as Figure 4B in the main text) was constructed by plotting the equilibrium average order parameter $\langle s \rangle$ as a function of α and γ . For all cases of $(\alpha$ and $\gamma)$ considered, we found that the order parameter plateaued around 3 different values of $\langle s \rangle$, given by $\langle s \rangle \approx 0.45$, $\langle s \rangle \approx 0.65$ and $\langle s \rangle \approx 0.95$. This is observed from Figure S19A, where we plot the average order parameter as a function of α and γ . By visualizing the orientations at different values of (γ, α) , we found that the typical orientations centered around the three different values of s were similar to each other, as shown in Figure 4C in the main text. From these results, we chose the phase-boundaries through $0.6 \leq \langle s \rangle \leq 0.85$ (diagonally aligned), $\langle s \rangle \leq 0.6$ (face-to-face aligned) and $\langle s \rangle > 0.85$ (edge-to-edge aligned). An additional step of Gaussian smoothing was performed to get the final phase diagram shown in Figure 4B.

The low effective temperature used for performing the MC simulation ensured that the resulting phase diagram primarily reflects the energetically preferred orientational order dictated by the free energy of the charge-layering. As a final step of validation, we compared the average free energies of some representative configurations sampled within each identified phase region and then compared the relative free energies between them. The phase diagram constructed by choosing the phase with the minimum free energy, plotted in Fig. S19B.

(D) Orientational order in a 32-site FCC Lattice. To ensure that our results, especially the emergence of edge-to-edge alignment at large screening length is not affected by finite size effects, we consider a $2 \times 2 \times 2$ FCC lattice with the same lattice constant of 90\AA as before that contains 32 NCs. For this system, we chose $\alpha = 3.0\text{\AA}$ and $\gamma = 1.1$, for which the 4-site results predicted the edge-to-edge aligned state to be favorable. The remaining parameters are chosen as $N_g = 180$, $b/a = 100\text{\AA}$, $\lambda/a = 500$, $k_B T = 50$ and $b/k_B T = 2\text{\AA}^{-2}$. As before, the orientations of all NCs are drawn randomly from the Haar distribution, and 50,000 Monte Carlo steps are performed to obtain the orientational order of the NCs in the super-lattice. Representative snapshots illustrating the system's evolution are presented chronologically in Fig. S19B. The simulation progresses from an initial random configuration towards states with increased orientational order and pronounced charge layering between the NCs. The final configuration after 50,000 MC steps, shown in Fig. S19B, clearly exhibits the edge-to-edge alignment predicted by the 4-site simulations and observed experimentally (Figure 4C main text), validating that our results are unaffected by finite size effects. The quantitative evolution towards this state is shown in Fig. S19B and S19B, which plot the average order parameter $\langle s \rangle$ (computed using Equation 5.13 averaged over 32 NCs) and the system free energy $F/k_B T$ versus MC steps, respectively. The order parameter rapidly increases towards $\langle s \rangle \approx 1$, while the free energy decreases and plateaus, indicating relaxation into the stable edge-to-edge aligned structure.

Finally, to ensure the stability of the observed phase is robust against the specific choice of numerical parameters, we performed additional validation simulations. Fig. S20E and S20F show the evolution of $\langle s \rangle$ and $F/k_B T$ for an identical simulation where the Lagrange multiplier enforcing the volume constraint was doubled ($\lambda/a = 1000$). The system clearly relaxes to the same high-order edge-to-edge state, confirming the result is not sensitive to the strength of this constraint.

5. SUPPORTING FIGURES

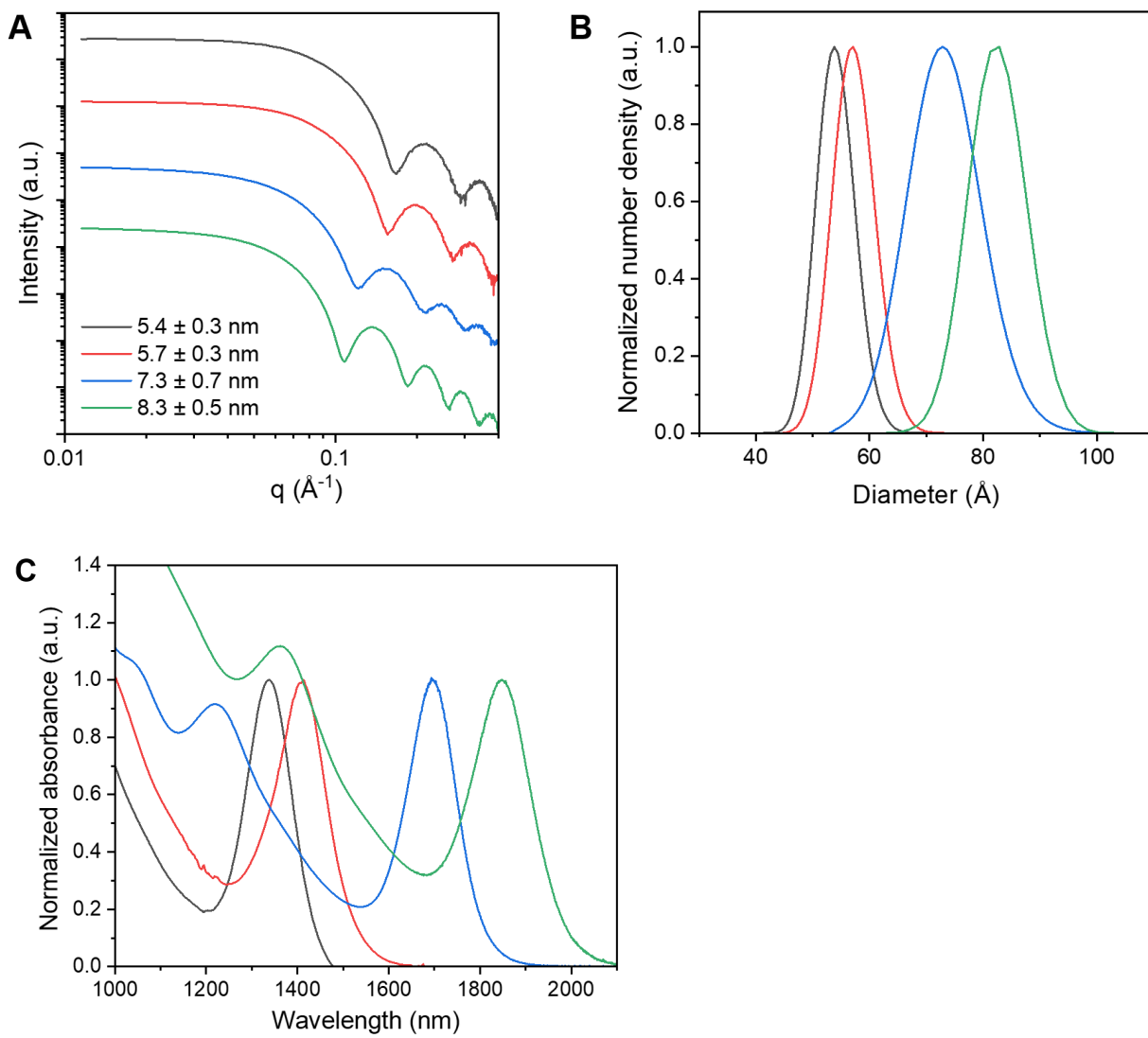


Figure S1. (A) SAXS patterns and (B) size distribution of 5.4, 5.7, 7.3 and 8.3 nm PbS-OA NCs. The standard deviations of the diameter are 0.3, 0.3, 0.7 and 0.5 nm, respectively. Each size distribution was obtained by fitting the form factor of the corresponding SAXS pattern (see Section 4.1). (C) UV-Vis spectra of the PbS-OA NCs.

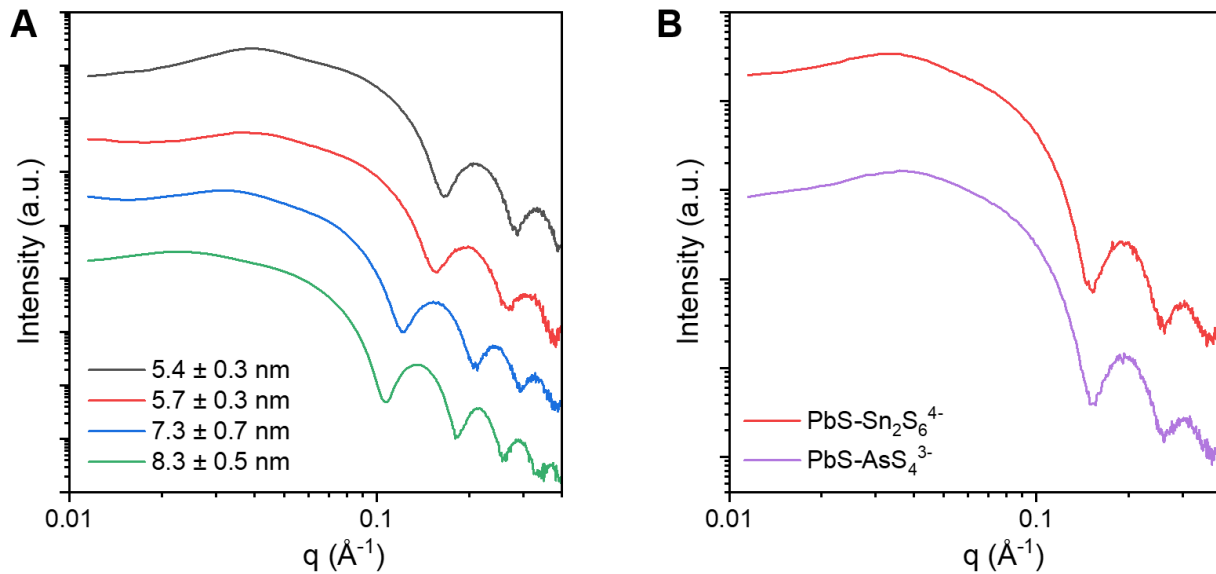


Figure S2. (A) SAXS patterns of $\text{PbS-Sn}_2\text{S}_6^{4-}$ NCs with various sizes and (B) SAXS patterns of 5.7 nm PbS NCs with various metal chalcogenide complex (MCC) ligands.

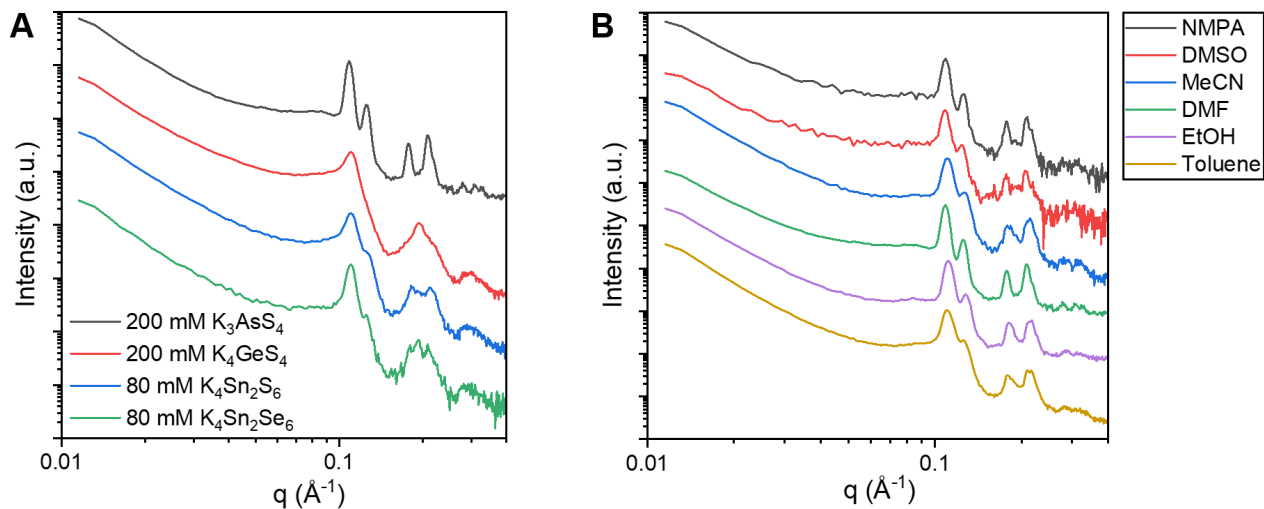


Figure S3. (A) SAXS patterns of 5.7 nm $\text{PbS-Sn}_2\text{S}_6^{4-}$ NCs that were self-assembled by adding 40% volume fraction of DMF as non-solvent and various salts as flocculants. (B) SAXS patterns of 5.7 nm $\text{PbS-Sn}_2\text{S}_6^{4-}$ NCs that were self-assembled by adding 200 mM of K_3AsS_4 as flocculant and 40% volume fraction of various organic solvents as non-solvents.

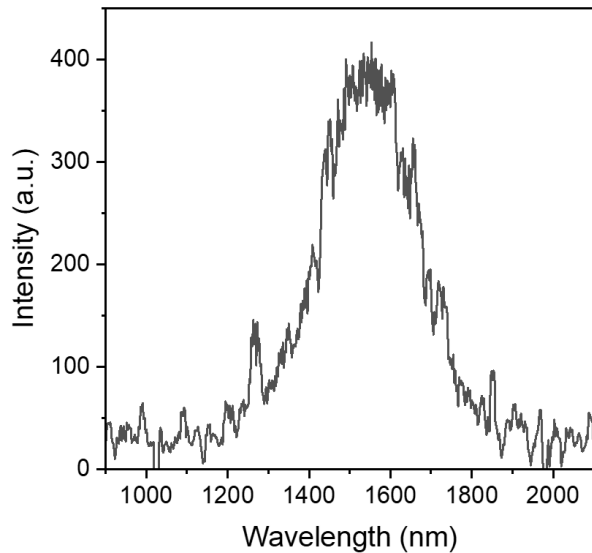


Figure S4. PL spectrum of 5.7 nm $\text{PbS-Sn}_2\text{S}_6^{4-}$ NC superlattice.

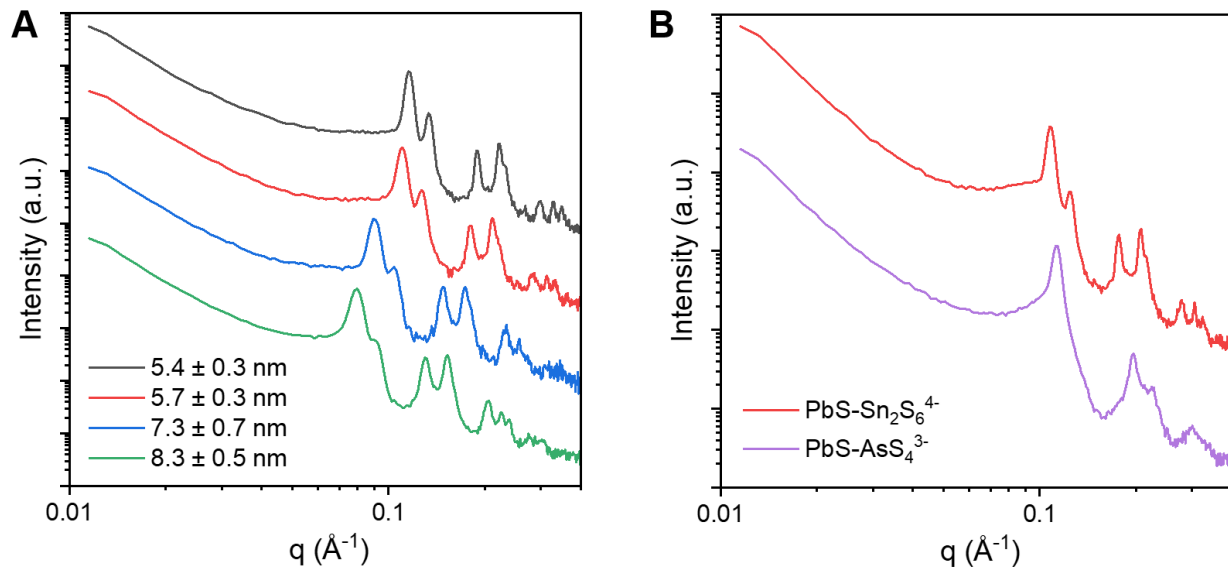


Figure S5. (A) SAXS pattern of superlattices of $\text{PbS-Sn}_2\text{S}_6^{4-}$ NCs with various sizes. (B) SAXS pattern of superlattices of 5.9 nm PbS NCs with various inorganic ligands.

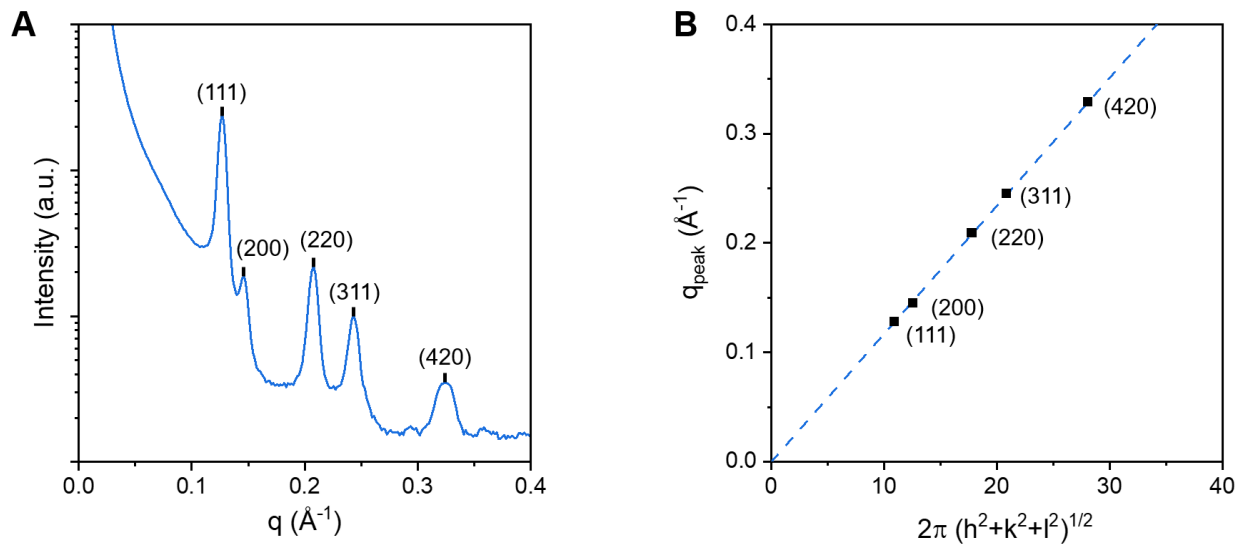


Figure S6. Plot of SAXS pattern (A) and the plot of q_{peak} versus $2\pi(h^2+k^2+l^2)^{1/2}$ of the superlattice of 5.7 nm $\text{PbS-Sn}_2\text{S}_6^{4-}$ NCs after washing with MeCN. The assigned Miller indices satisfy the selection rule for an *fcc* crystal structure (where h , k , and l are either all odd or all even). The data points align closely with a straight line passing through the origin, confirming that the superlattices exhibit an *fcc* structure.

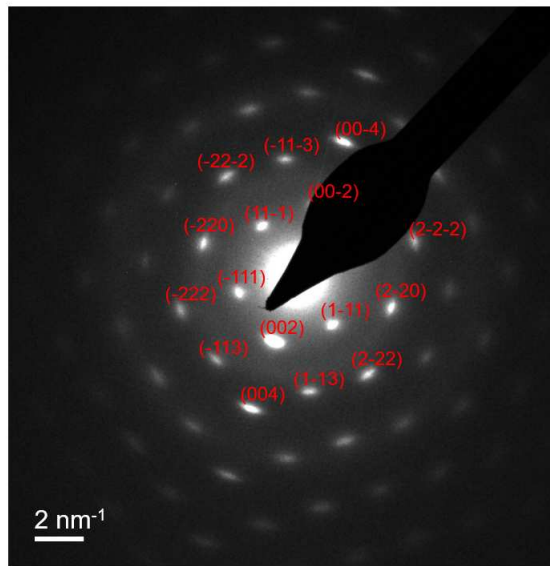


Figure S7. Spot assignment of an SAED image of 5.7 nm $\text{PbS-Sn}_2\text{S}_6^{4-}$ NC superlattice, shown in main text Figure 1C.

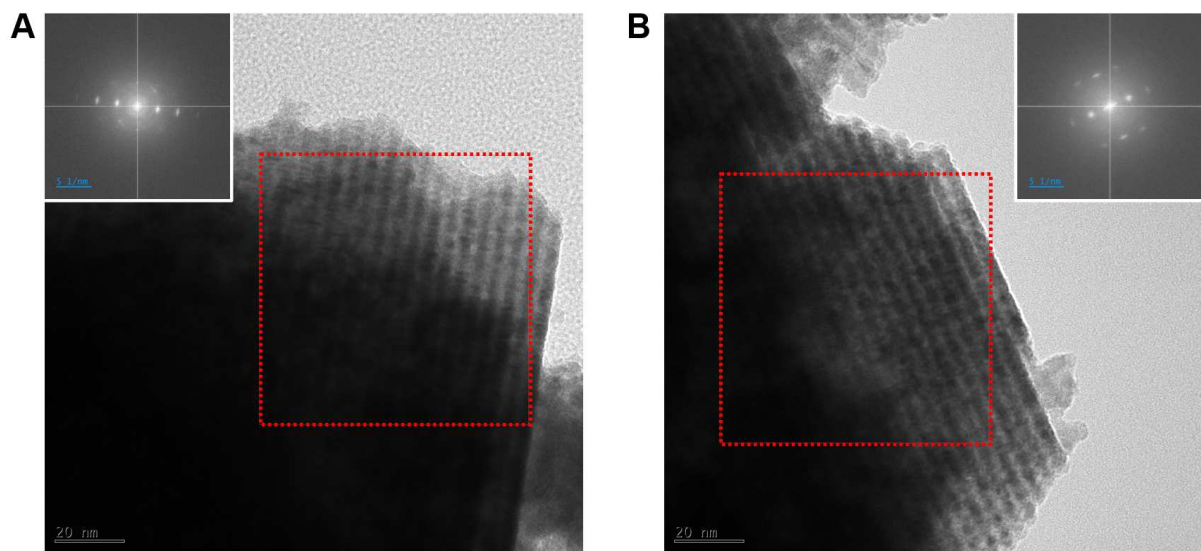


Figure 8. TEM image of (A) as-prepared and (B) washed 5.7 nm $\text{PbS-Sn}_2\text{S}_6^{4-}$ NC superlattices. Fourier transformed images of the areas highlighted in red boxes are shown in the inset.

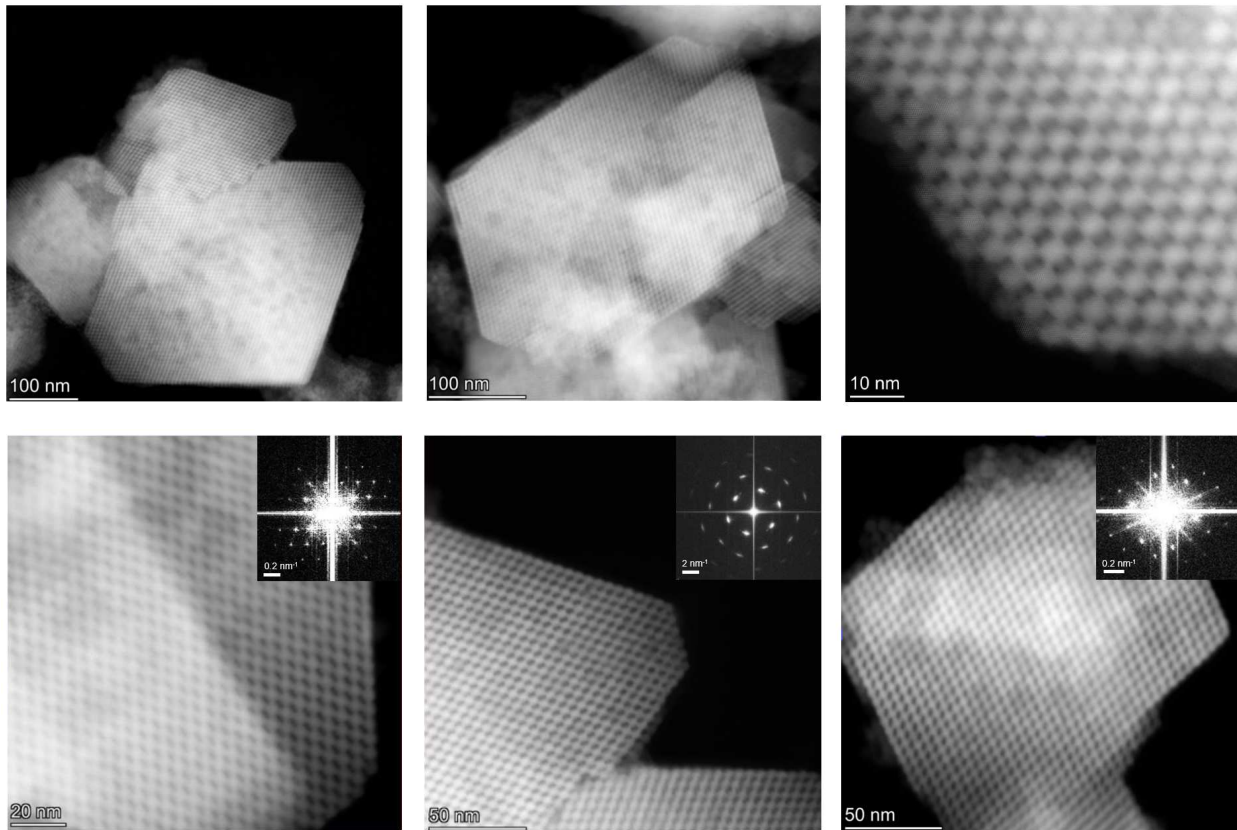


Figure S9. HAADF-STEM images of 5.7 nm $\text{PbS-Sn}_2\text{S}_6^{4-}$ NC superlattices. Insets: Fourier transformed image of the corresponding STEM images.

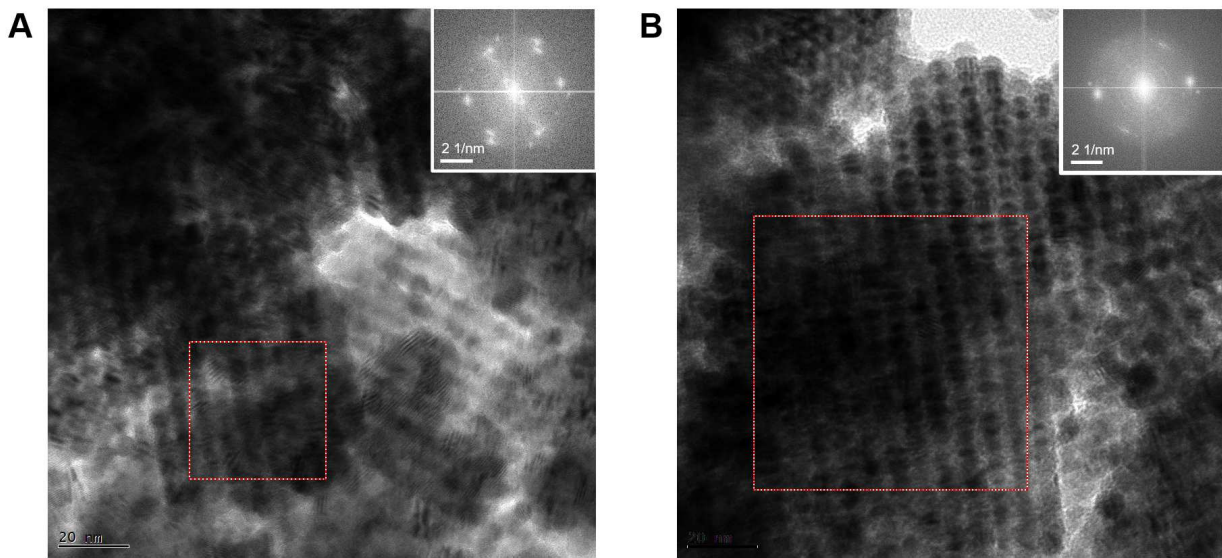


Figure S10. TEM images of (A) 7.3 nm and (B) 8.3 nm $\text{PbS-Sn}_2\text{S}_6^{4-}$ NC superlattices. Inset: Fourier transformed image of the region enclosed by red dashed box. The distinct spot patterns in wide-angle FT-TEM images shown in the inset indicate that there is a strong preference for the NCs to be orientationally aligned within the superlattice.

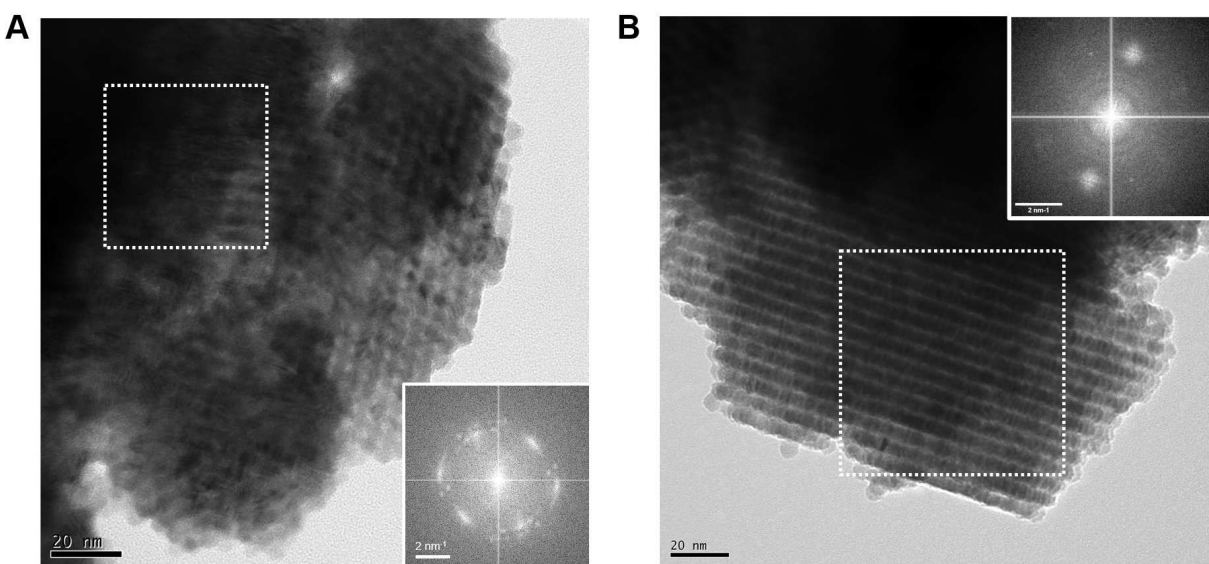


Figure S11. HRTEM image of the superlattice of (A) 5.7 nm PbS-AsS_4^{3-} and (B) 6.4 nm $\text{PbSe-Sn}_2\text{S}_6^{4-}$ NCs. Inset: Fourier transformed image of the region enclosed by white dashed box.

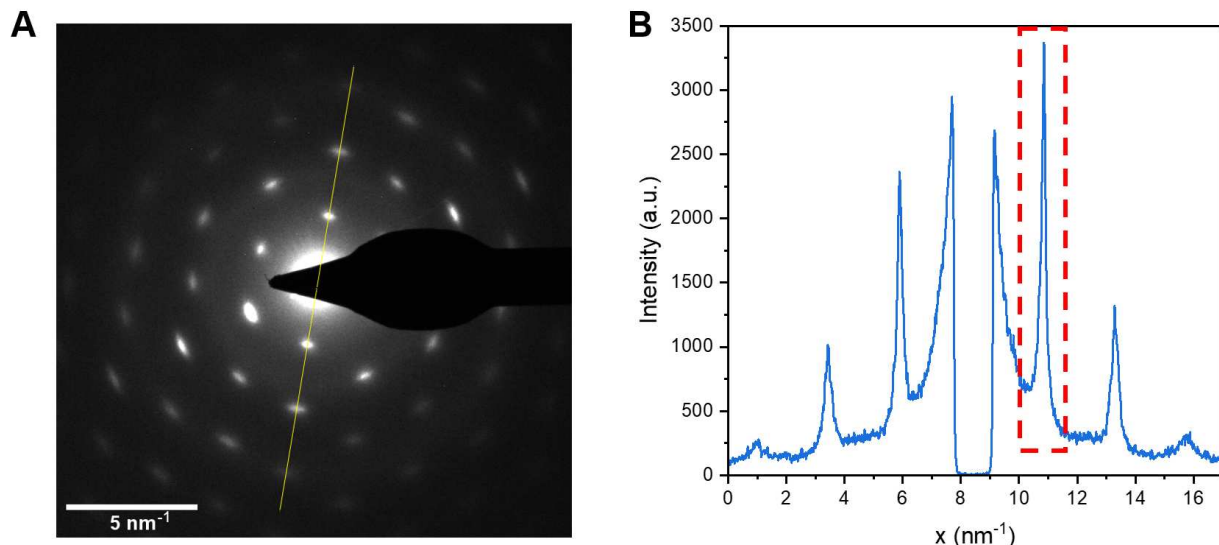


Figure S12. (A) SAED image of the 5.7 nm $\text{PbS-Sn}_2\text{S}_6^{4-}$ NC superlattice. The yellow line indicates the location where the linear profile shown in (B) is obtained. The peak indicated by the dashed red box in (B) is the peak where the full-width half-maximum (FWHM) was obtained for the Scherrer analysis. The detailed description of the Scherrer analysis is given in Section 4.2.

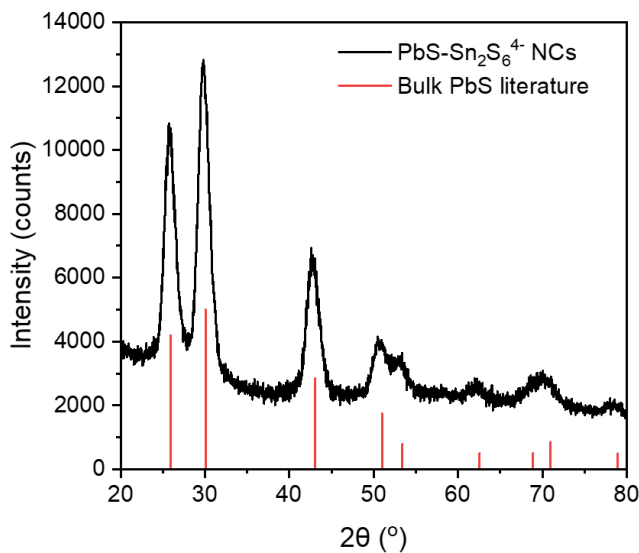


Figure S13. PXRD pattern of PbS NCs. The lines are the PXRD pattern of bulk PbS obtained from the literature (rock-salt structure, unit cell length 5.9 \AA). Details of the Wulff construction analysis are presented in Section 4.2.

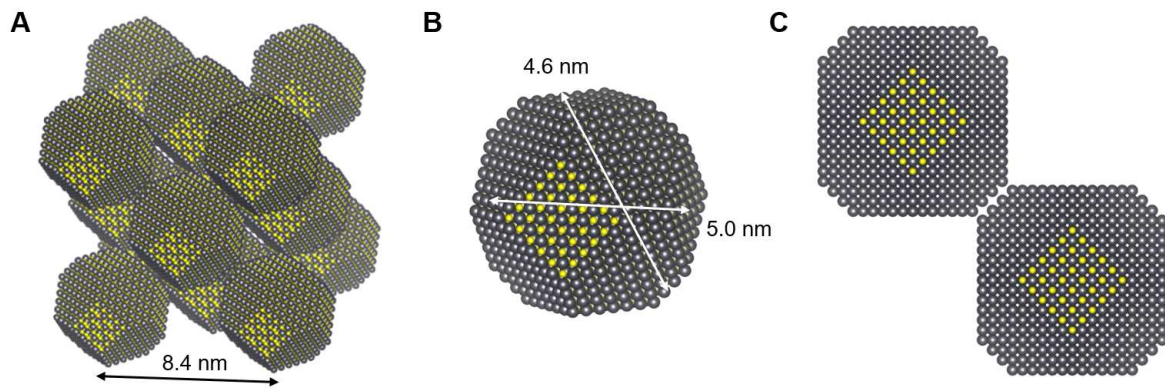


Figure S14. Illustration of $\text{PbS-Sn}_2\text{S}_6^{4-}$ NC (A) superlattice and (B) nanocrystal for simulating the scattering pattern. The atomic edges of the NCs are precisely aligned, as illustrated in (C). Details of the simulation are in Section 4.2 of the SI.

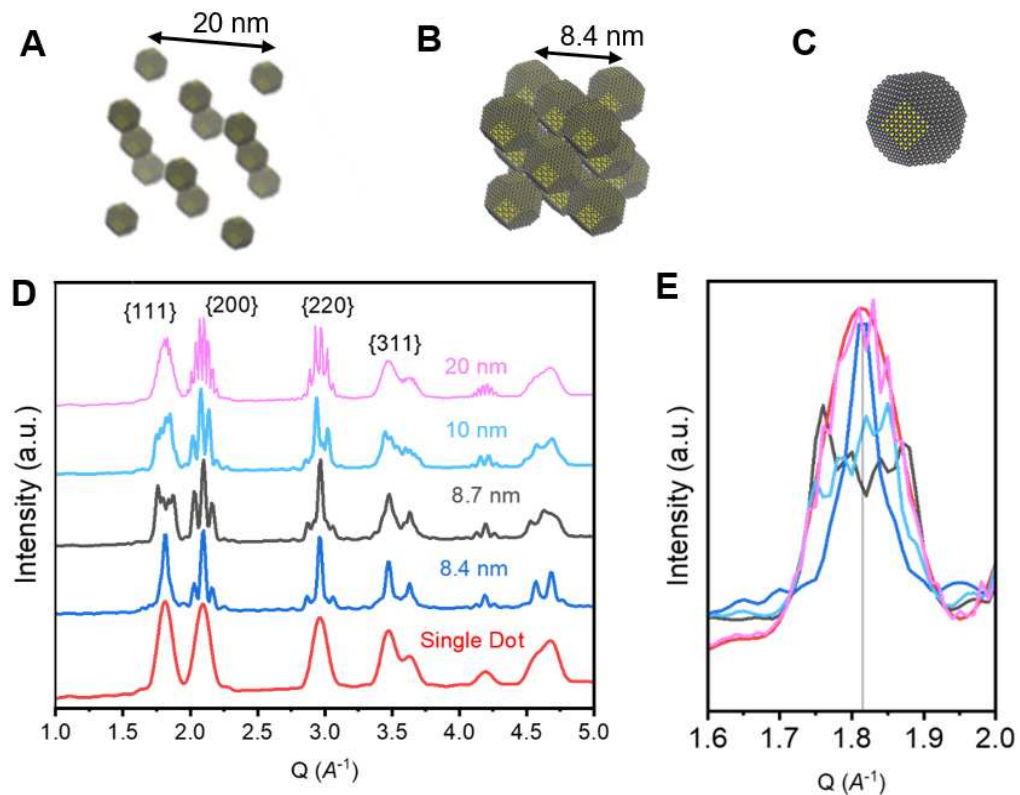


Figure S15. Illustration of $\text{PbS-Sn}_2\text{S}_6^{4-}$ NC superlattice with the lattice constant of (A) 20 nm and (B) 8.4 nm. (C) presents the illustration of a single $\text{PbS-Sn}_2\text{S}_6^{4-}$ NC particle. (D) Simulated scattering pattern of $\text{PbS-Sn}_2\text{S}_6^{4-}$ NC superlattices with varying lattice constant and a single NC particle. (E) Enlarged image of [111] peak. Details of the simulation are in Section 4.2.

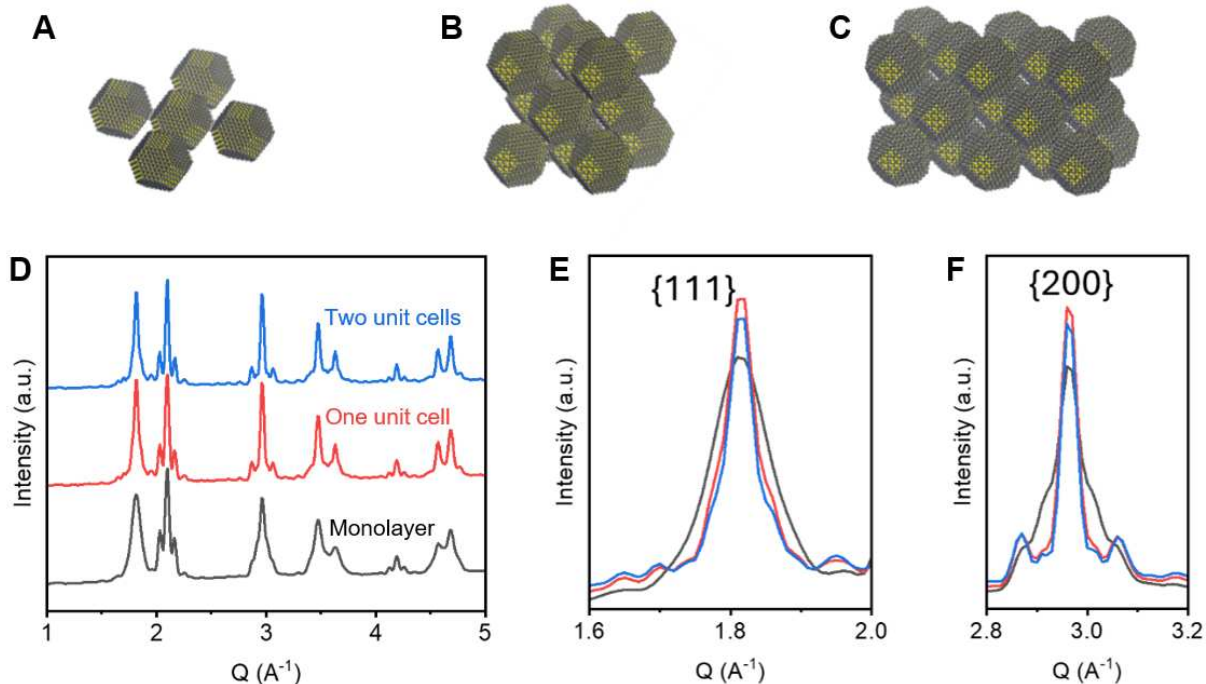


Figure S16. Illustration of (A) one monolayer, (B) one unit cell and (C) two unit cells of PbS-Sn₂S₆⁴⁻ NC superlattice. (D) Simulated scattering pattern of PbS-Sn₂S₆⁴⁻ NC superlattices with different numbers of repeating units. Also shown are enlarged scattering patterns of (E) the {111} peak and (F) the {200} peak. Details of the simulation are in Section 4.2.

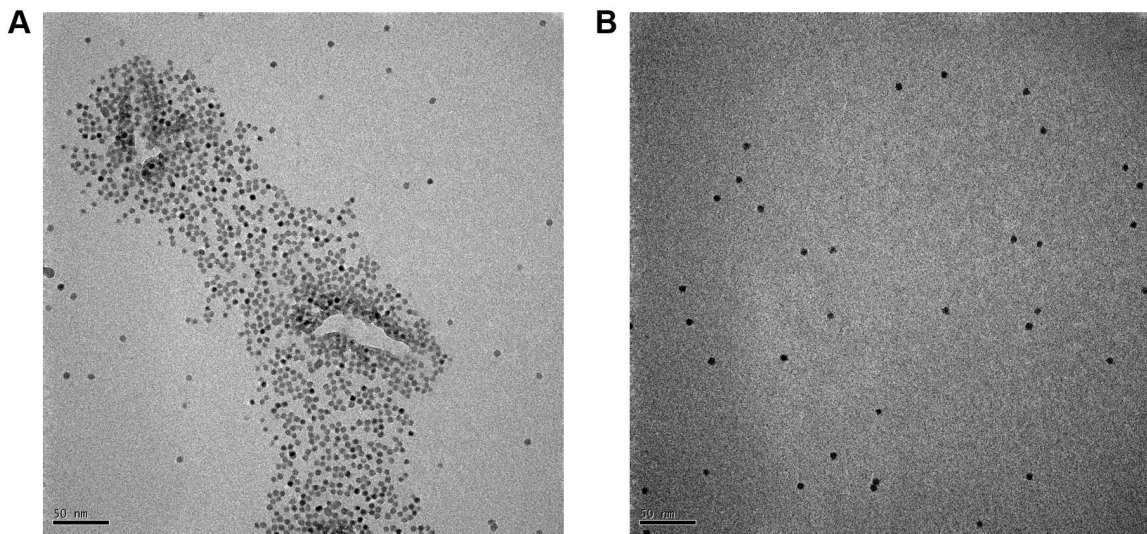


Figure S17. TEM images of 5.7 nm PbS-Sn₂S₆₄₋ NCs. (A) and (B) are taken from a same sample but at different spots.

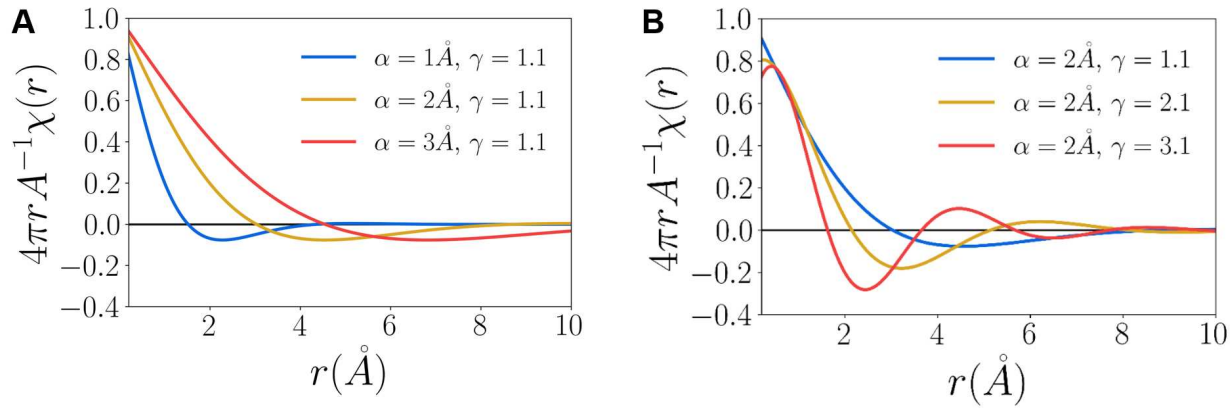


Figure S18. Plots of theoretically calculated susceptibility of 5.7 nm nanoparticles with varied values of (A) α and (B) γ .

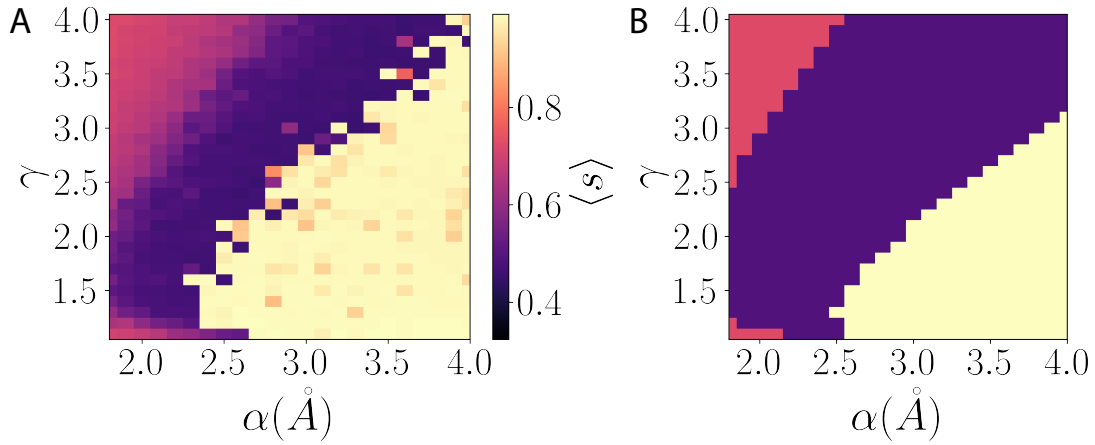


Figure S19. (A) Average values of the order parameter $\langle s \rangle$ obtained from Monte Carlo production runs. (B) Phase diagram constructed by comparing the free energy of representative orientations in each of the three phases, exhibiting consistency with Figure 4B in the main text. The pink, purple and yellow regions correspond to diagonal orientation, face-to-face orientation and edge-to-edge orientation, respectively. Illustrations of these orientational phases can be found in Figure 4C.

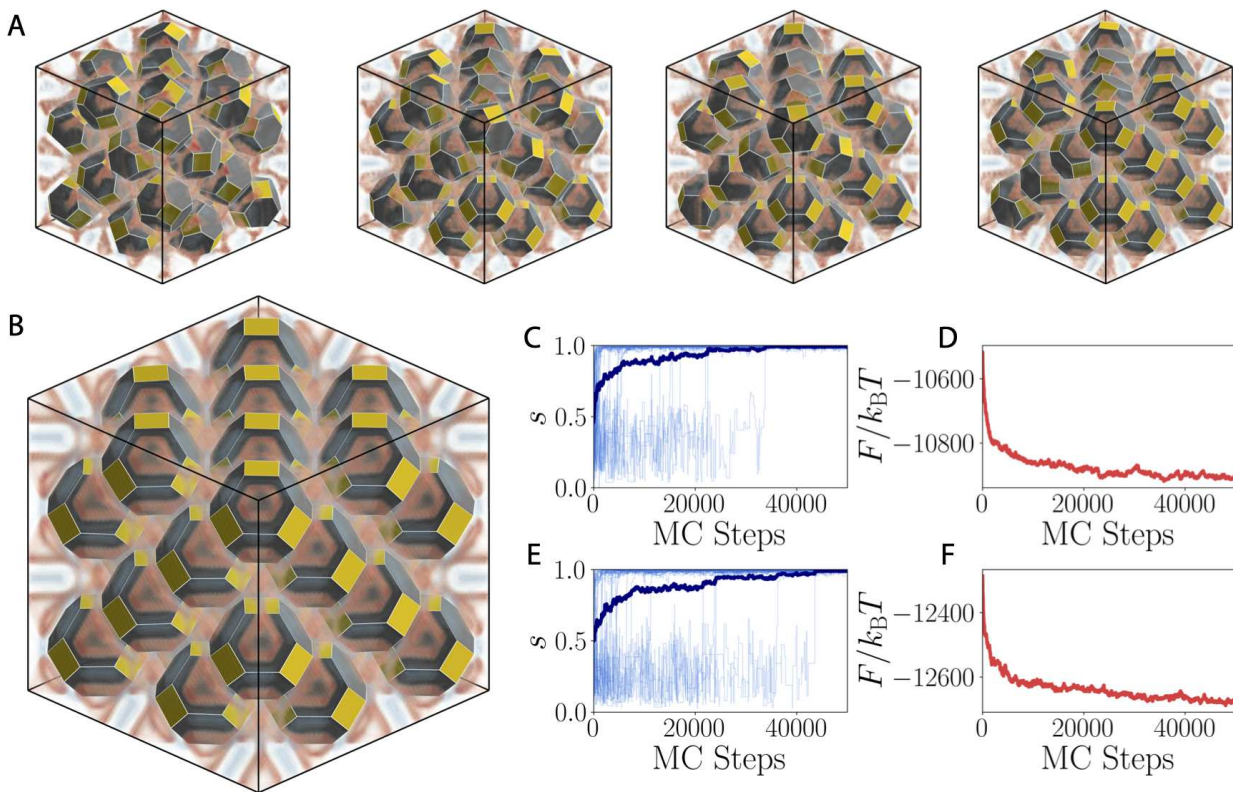


Figure S20. Validation of orientational ordering in a $2 \times 2 \times 2$ FCC lattice (32 NCs) via Monte Carlo simulation (using $\alpha = 3.0 \text{ \AA}$, $\gamma = 1.1$). (A) Snapshots from the Monte-Carlo simulation for the $2 \times 2 \times 2$ FCC lattice, arranged chronologically from left to right. (B) Final snapshot of the Monte-Carlo run, with NCs showing edge-to-edge alignment, consistent with the charge layering depicted in Fig. 3E in the main text. (C) Value of the order parameter s defined in Eq. 16 for the 32 NC (semi-transparent) and the average (opaque) as a function of Monte-Carlo steps. (D) Corresponding evolution of the system's free energy. (E,F) Equivalent plots to (C,D) from a simulation where the Lagrange multiplier λ (enforcing volume constraints) was doubled, confirming the robustness of the relaxation to the ordered state.

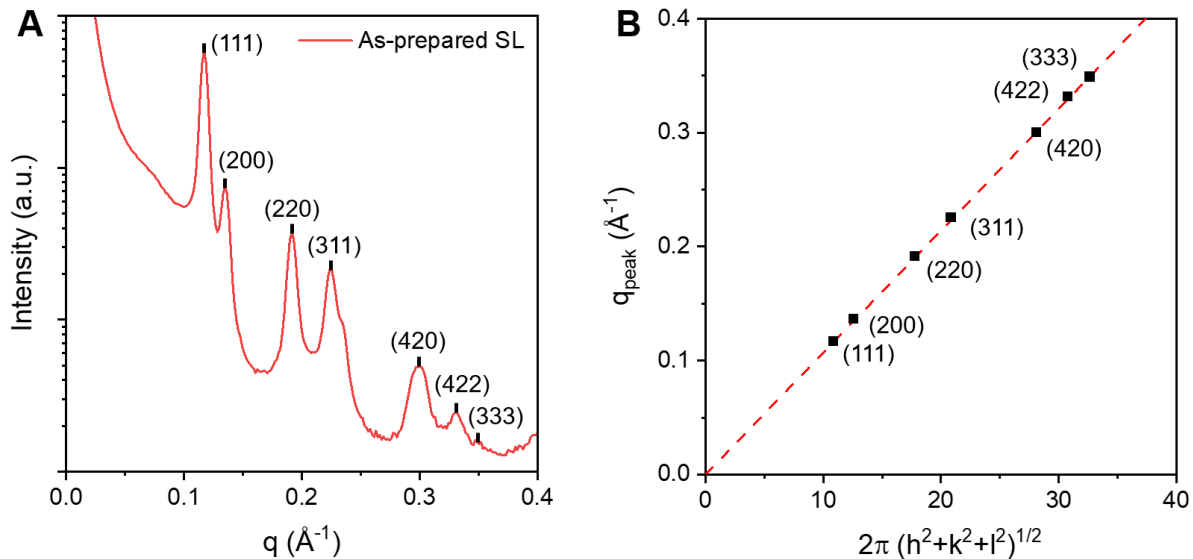


Figure S21. (A) SAXS pattern of as-prepared superlattice of 5.7 nm $\text{PbS-Sn}_2\text{S}_6^{4-}$ NCs with peak assignment. The superlattice was deposited on Kapton tape and dried before the SAXS measurement. (B) Peak analysis of the superlattice.

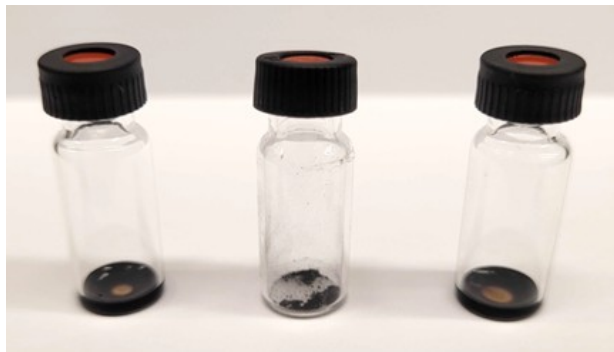


Figure S22. Photograph of colloidal 5.7 nm $\text{PbS-Sn}_2\text{S}_6^{4-}$ NCs (left), superlattices in powdered form (center), and colloidal NCs that are recovered by redispersing superlattices in NMF (right).

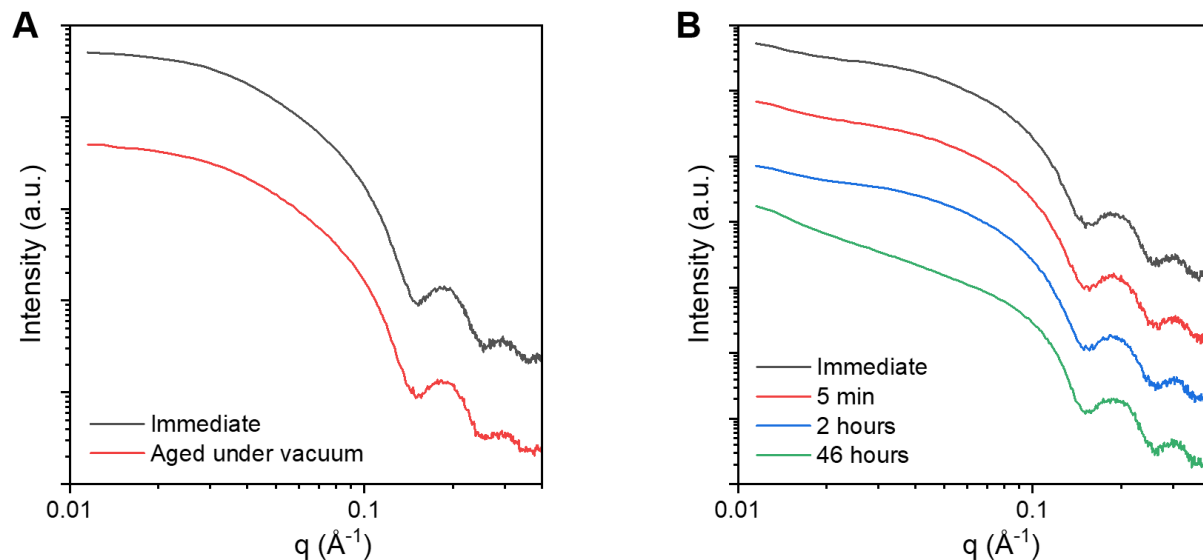


Figure S23. SAXS patterns of as-prepared 5.7 nm $\text{PbS-Sn}_2\text{S}_6^{4-}$ NC superlattices redispersed in NMF. (A) Superlattices were redispersed in NMF immediately after solvent removal or after drying under vacuum for 2 hours. (B) Superlattices were stored under a N_2 atmosphere for the indicated durations following solvent removal and subsequently redispersed in NMF.



Figure S24. TEM images of (A) original colloid, (B) superlattice and (C) redispersed colloid of 5.7 nm $\text{PbS-Sn}_2\text{S}_6^{4-}$ NCs.

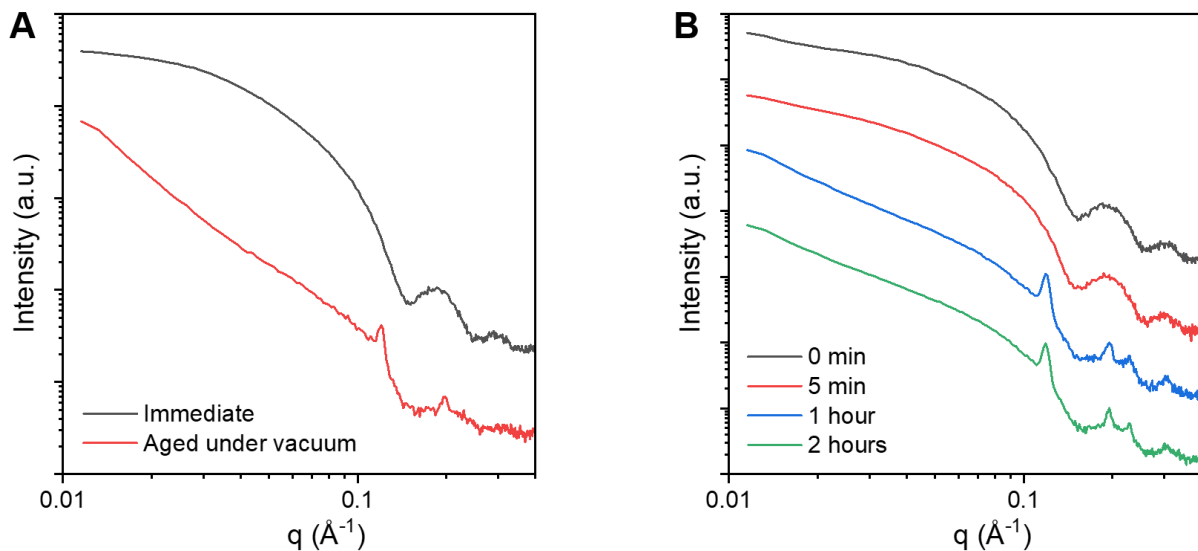


Figure S25. SAXS patterns of washed 5.7 nm $\text{PbS-Sn}_2\text{S}_6^{4-}$ NC superlattices redispersing in NMF. **(A)** Superlattices were redispersing in NMF immediately after solvent removal or after drying under vacuum for 2 hours. **(B)** Superlattices were stored under a N_2 atmosphere for the indicated durations following solvent removal and subsequently redispersing in NMF.

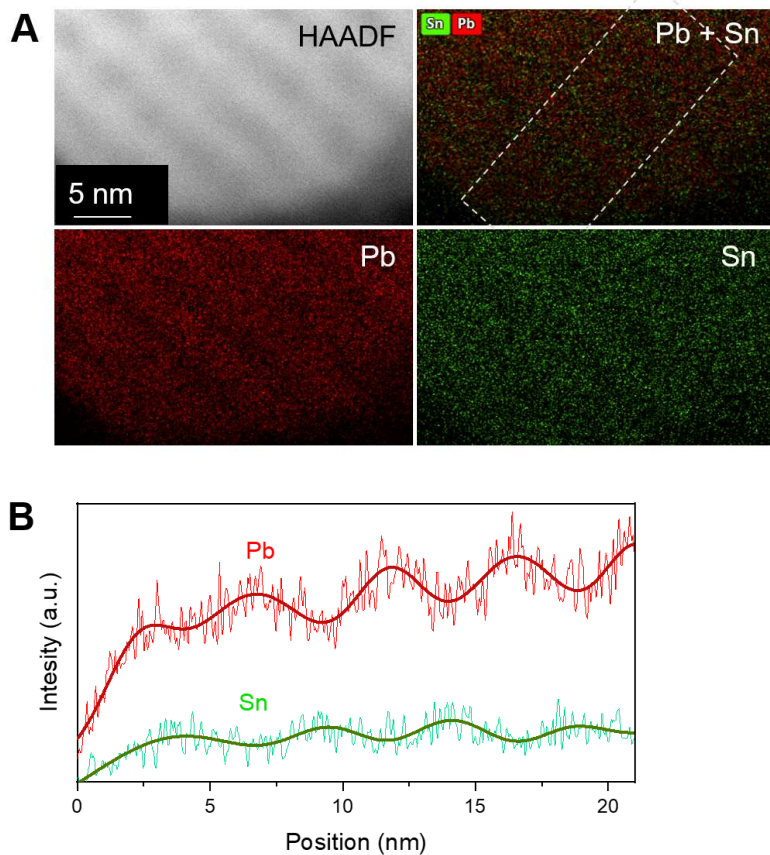


Figure S26. **(A)** HAADF-STEM image and STEM-EDS mapping of 5.9 nm $\text{PbS-Sn}_2\text{S}_6^{4-}$ NC superlattice. **(B)** Line scan of the STEM-EDS mapping. The area where the line scan was carried out is marked with a dashed grey box. **(C)** Intensity counts of S, As and Sn relative to the intensity count of Pb on a line scan of STEM-EDS of 5.9 nm $\text{PbS-Sn}_2\text{S}_6^{4-}$ NC superlattice.

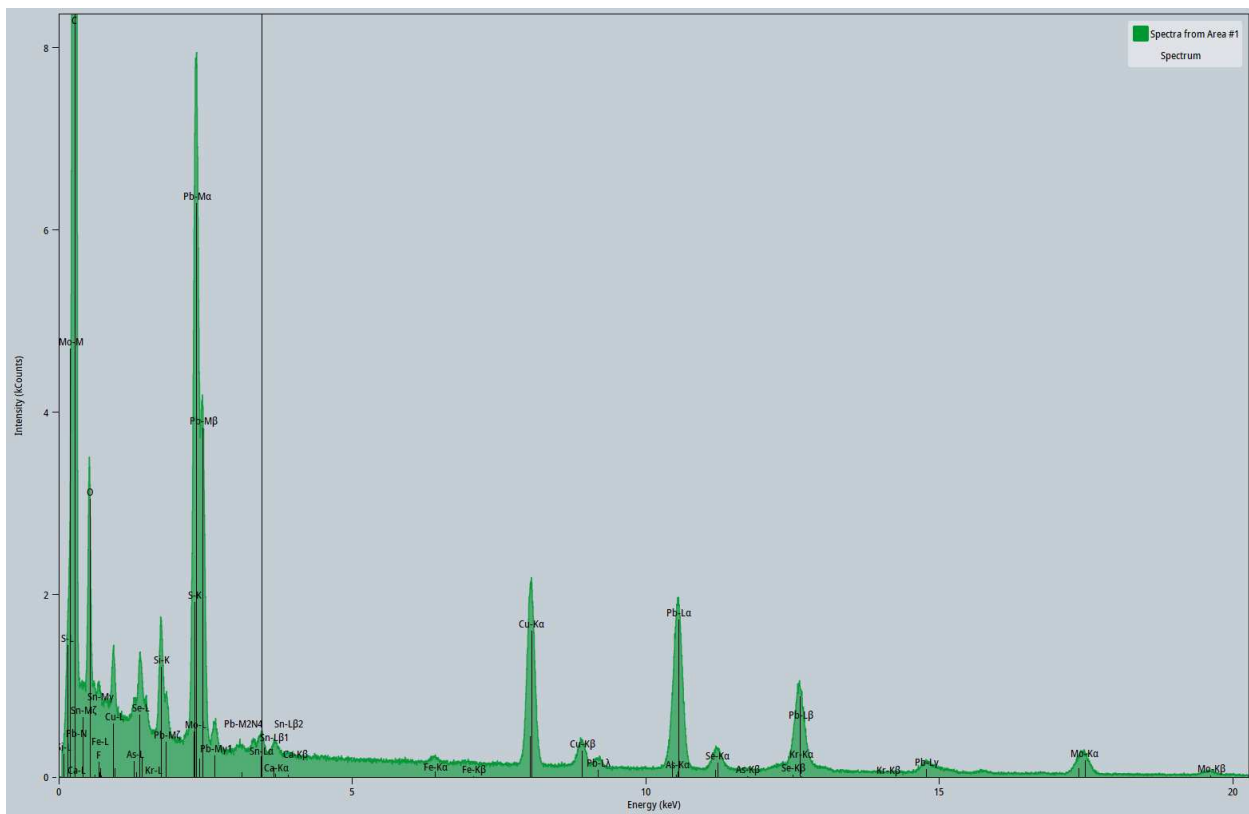


Figure S27. Accumulative STEM-EDS spectrum of 5.9 nm $\text{PbS-Sn}_2\text{S}_6^{4-}$ NC superlattice. The HAADF-STEM image and STEM-EDS mapping of the region where this EDS spectrum is taken can be found in Figure 5E in the main text and Figure S26. The origin of other elements is as follows: Cu from TEM grid, Fe from TEM, Mo from TEM holder and Se from EDS detector. Ca and Si are commonly found impurities from air dust.

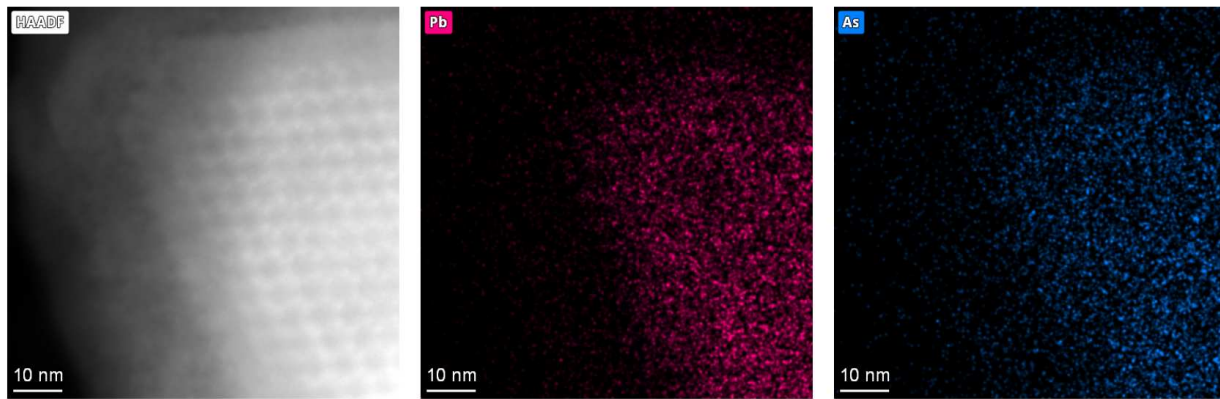


Figure S28. HAADF-STEM image and STEM-EDS images of unwashed 5.9 nm $\text{PbS-Sn}_2\text{S}_6^{4-}$ NC superlattices.

6. SUPPORTING TABLES

Table S1. Relative mole ratio of five elements (Pb, S, K, Sn, As) in 5.7 nm $\text{PbS-Sn}_2\text{S}_6^{4-}$ NC superlattices before and after washing with MeCN, obtained through the ICP-OES measurements.

Element	NC solution	Before wash	After wash
Pb	1.000	1.000	1.000
S	1.131	1.190	1.122
K	0.137	0.277	0.222
Sn	0.094	0.074	0.072
As	None	0.086	0.065

[1] Kovalenko, M.; Scheele, M.; Talapin, D. Colloidal Nanocrystals with Molecular Metal Chalcogenide Surface Ligands. *Science* **2009**, *324*, 1417–1420.

[2] Kovalenko, M.; Bodnarchuk, M.; Zaumseil, J.; Lee, J.-S.; Talapin, D. Expanding the Chemical Versatility of Colloidal Nanocrystals Capped with Molecular Metal Chalcogenide Ligands. *J. Am. Chem. Soc* **2010**, *132*, 10085–10092.

[3] Jeong, A.; Portner, J.; Tanner, C.; Ondry, J.; Zhou, C.; Mi, Z.; Tazoui, Y.; Lee, B.; Wall, V.; Ginsberg, N.; Talapin, D. Colloidal Dispersions of Sterically and Electrostatically Stabilized PbS Quantum Dots: Structure Factors, Second Virial Coefficients, and Film-Forming Properties. *ACS Nano* **2024**, *18*, 33864–33874.

[4] Zaluzec, N. First Light on the Argonne PicoProbe and the X-Ray Perimeter Array Detector (XPAD). *Microscopy and Microanalysis* **2021**, *27*, 2070–2074.

[5] Smilgies, D.-M. Scherrer Grain-Size Analysis Adapted to Grazing-Incidence Scattering with Area Detectors. *J. Appl. Crystallogr* **2009**, *42*, 1030–1034.

[6] Toso, S.; Baranov, D.; Altamura, D.; Scattarella, F.; Dahl, J.; Wang, X.; Marras, S.; Alivisatos, A.; Singer, A.; Giannini, C.; Manna, L. Multilayer Diffraction Reveals That Colloidal Superlattices Approach the Structural Perfection of Single Crystals. *ACS Nano* **2021**, *15*, 6243–6256.

[7] Trigg, E. <https://github.com/etrigg/DebyeByPy>., Accessed January 2026.

[8] Shklovskii, B. Screening of a Macroion by Multivalent Ions: Correlation-Induced Inversion of Charge. *Phys. Rev. E* **1999**, *60*, 5802–5811.

[9] Zhang, H.; Dasbiswas, K.; Ludwig, N.; Han, G.; Lee, B.; Vaikuntanathan, S.; Talapin, D. Stable Colloids in Molten Inorganic Salts. *Nature* **2017**, *542*, 328–331.

[10] Limmer, D. T. Interfacial Ordering and Accompanying Divergent Capacitance at Ionic Liquid-Metal Interfaces. *Phys. Rev. Lett.* **2015**, *115*, 256102.

[11] Fredrickson, G. H. Surface ordering phenomena in block copolymer melts. *Macromolecules* **1987**, *20*, 2535–2542.

[12] Wuttke, J. Numerically stable form factor of any polygon and polyhedron. *Applied Crystallography* **2021**, *54*, 580–587.

[13] Lee, S.-W.; Mittra, R. Fourier transform of a polygonal shape function and its application in electromagnetics. *IEEE Transactions on Antennas and Propagation* **1983**, *31*, 99–103.